

Theory of unconventional magnetism in a Cu-based kagome metal

Anja Wenger,¹ Armando Consiglio,² Hendrik Hohmann,¹ Matteo Dürrnagel,^{1,3,*} Fabian O. von Rohr,⁴ Harley D. Scammell,⁵ Julian Ingham,⁶ Domenico Di Sante,⁷ and Ronny Thomale^{1,†}

¹*Institut für Theoretische Physik und Astrophysik and Würzburg-Dresden Cluster of Excellence ct.qmat, Universität Würzburg, 97074 Würzburg, Germany*

²*Istituto Officina dei Materiali, Consiglio Nazionale delle Ricerche, Trieste I-34149, Italy*

³*Institute for Theoretical Physics, ETH Zürich, 8093 Zürich, Switzerland*

⁴*Department of Quantum Matter Physics, University of Geneva, CH-1211 Geneva, Switzerland*

⁵*School of Mathematical and Physical Sciences, University of Technology Sydney, Ultimo, NSW 2007, Australia*

⁶*Department of Physics, Columbia University, New York, NY, 10027, USA*

⁷*Department of Physics and Astronomy, University of Bologna, 40127 Bologna, Italy*

(Dated: November 6, 2025)

Kagome metals have established a new arena for correlated electron physics. To date, the predominant experimental evidence centers around unconventional charge order, nematicity, and superconductivity, while magnetic fluctuations due to electronic interactions, i.e., beyond local atomic magnetism, have largely been elusive. We find the challenge of locating the appropriate parameter regime for such exotic order to center around two aspects. First, the correlations implied by low-energy orbitals have to be sufficiently large to yield a dominance of magnetic fluctuations and weak to retain an itinerant parent state. Second, the kinematic kagome profile at the Fermi level demands an efficient mitigation of sublattice interference causing the suppression of magnetic fluctuations descending from electronic on-site repulsion. We elucidate our methodology by analyzing the potential copper-based kagome compound CsCu_3Cl_5 : From *ab initio* design and many-body analysis, we develop a model framework of realistic Cu-based kagome materials the simulations of which reveal unconventional magnetic order in a kagome metal.

Introduction The kagome lattice, characterized by its repeating pattern of corner-sharing triangles, forms a hexagonal network with three distinct sublattices. This unique geometry gives rise to exotic quantum phenomena, rendering it an exclusive host for correlated and topologically nontrivial electronic states. Depending on the balance between electronic interactions and kinetic energy, electronic models on the kagome lattice can yield myriad distinct physical phases. Kagome compounds with a metallic parent state generically feature intricate non-magnetic phases such as exotic charge orders, nematicity and superconductivity [1–6]. Most extensively discussed is the AV_3Sb_5 family ($A=\text{K,Rb,Cs}$), in which the lack of magnetic order is best explained by both electron-phonon coupling effects [7, 8] and the suppression of on-site Coulomb repulsion due to the sublattice interference (SI) mechanism, preventing local scattering channels between the van Hove singularities (vHS) [9–11]. This leads to a rich zoology of unconventional phases like charge bond (CBO) and loop current orders (LCO), which are largely not found in alternative correlated electron material domains such as cuprate or iron-pnictide compounds [12–14]. Due to the predominance of non-magnetic phases, however, magnetic instabilities that might be unique to kagome kinematics have remained largely unexplored at the microscopic and even at the phenomenological level.

The emergence of magnetic instabilities requires a sufficient degree of electronic correlations. For strong electron-electron interactions, the electrons become Mott-localized on atomic sites, where unpaired spins cre-

ate magnetic moments. The inherent geometric frustration of the kagome lattice leads to unconventional magnetic orders such as spin liquid phases. The most prominent example is Herbertsmithite ($\text{ZnCu}_3(\text{OH})_6\text{Cl}_2$) [15, 16], which lies deep in the Mott-insulating regime, rendering the unique features of the kagome band structure like vHS and Fermi surface nesting – which drive unconventional charge order in the itinerant case – irrelevant.

In this article, we aim to fuse the intricacies of electronic kagome kinematics with the potential emergence of magnetic order. We identify intermediately correlated kagome compounds close to the mixed m -type van Hove filling as a suitable system to stabilize exotic magnetic orders, that inherit substantial non-local spin expectation values from the partial sublattice polarization of the Fermi surface. From detailed electronic structure calculations we find that Cu-based 135-kagome compounds, i.e. CsCu_3Cl_5 , provide a playground for exploring the potential realization of unconventional magnetic order in a realistic material setting. The low-energy physics of CsCu_3Cl_5 is well described by an isolated set of three bands with an m -type vHS close to the Fermi level and exhibits correlations intermediate between Herbertsmithite and the weakly correlated AV_3Sb_5 compounds. While Cu-O complexes are likely to be located in the Mott-localized regime, we propose Cu-Cl complexes strike the aspired compromise between maximum interaction strength while preserving metallicity. Our analysis of the magnetic phase diagram unveils CsCu_3Cl_5 as a realistic material platform to host correlation-driven spin-bond order and highlights the broader implications

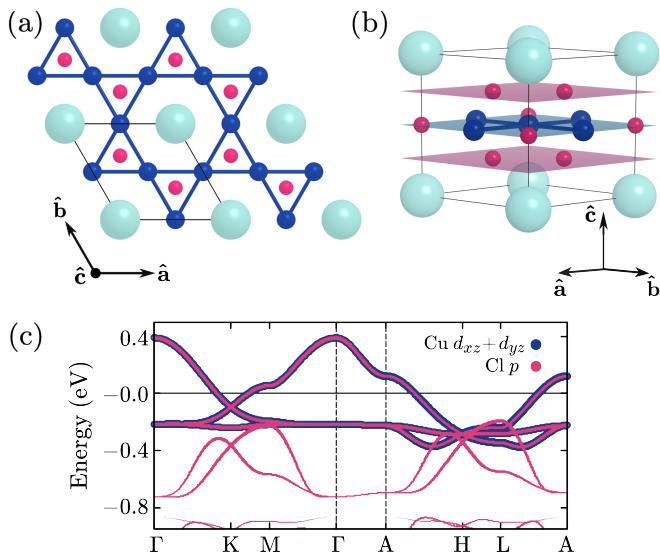


FIG. 1. Crystal structure of pristine CsCu_3Cl_5 . (a) Top view showing the Cu kagome lattice highlighted by blue bonds. Turquoise, blue and pink spheres represent Cs, Cu and Cl atoms. The unit cell is delimited by black lines. (b) Side view of the unit cell. The blue plane contains the Cu kagome lattice and additional Cl atoms, while the pink planes above and below contain a hexagonal lattice of Cl atoms. (c) Electronic band structure with projected orbital weights featuring distinct kagome bands and an m -type vHS close to E_F .

of Fermi surface topology for exotic magnetic phases in kagome systems.

Model Realization Our theoretical platform CsCu_3Cl_5 is isostructural with other members of the 135 family, such as AV_3Sb_5 , and crystallizes in the hexagonal space group $P6/mmm$ (No. 191). It features an in-plane kagome network of copper atoms, coordinated octahedrally by chlorine atoms, forming layered Cu_3Cl_5 sheets that are separated along the \hat{c} -axis by a triangular net of cesium ions. CsCu_3Cl_5 exhibits a mixed valence state, where copper ions are present in both Cu(I) and Cu(II) oxidation states, with an average oxidation state of +1.33.

While Cu generally prefers the +II oxidation state, as observed in the chemically related phases Cs_2CuCl_4 [17] and CsCuCl_3 [18], the presence of Cu(I) in compounds such as $\text{Cs}_3\text{Cu}_2\text{Cl}_5$ [19] supports the feasibility of this mixed valence state. A notable point is the possibility of a mixed charge on a crystallographic site. Whether this is statistically distributed in the structural model or whether some form of ordering is present remains an open question. The ionic radii of Cu(I) and Cu(II) in octahedral coordination do not differ significantly, making this mixed occupation proposed here certainly plausible [20]. Due to its full d^{10} electron configuration, Cu(I) lacks the electronic degeneracy needed for Jahn-Teller distortions, making it less prone to such distortions compared to Cu(II). In contrast, Cu(II), with its d^9 electron configuration, is a well-known Jahn-Teller ion and typically

undergoes bond elongations or compressions in its octahedral coordination environment to lower its energy [21]. It is also worth noting that Cu(I), at least in chloride environments, does not always form regular coordination polyhedra. This irregularity might stem from the nature of Cs-Cl compounds, where the large size of Cs ions can sometimes influence the coordination environments of surrounding atoms, though such effects are less likely in layered structures like those in CsCu_3Cl_5 . A thorough analysis of the compound's stability reveals the pristine configuration as a metastable state. However, the analysis of single particle and derived many-body effects in the energetically favored twisted configuration matches qualitatively the results for the pristine case. To maintain generality, we explicate in the following a study of the pristine structure and refer the interested reader to the SM for the analogous treatment of the twisted configuration.

Despite being isostructural to other members of the 135 family like AV_3Sb_5 , the calculated electronic band structure, shown in Fig. 1(c), reveals striking differences to previous reports on known kagome compounds. The characteristic kagome band manifold – including a flat band, a Dirac point located at the K-point, and two vHSs at each of the three inequivalent M-points – appears well separated from other bands at low energies. The orbital projection of the bandstructure illustrates that the states at E_F emerge only from the hybridization of the out-of-plane Cu d_{xz} and d_{yz} orbitals with Cl p orbitals. This can be attributed to a collaborative effect: The enhanced valence of Cu (d^9) suggests a single kagome band manifold close to the Fermi level in analogy to ATi_3Bi_5 ($A = \text{Cs, Rb}$) [22–24], where the d^1 configuration of Ti constitutes the analogue of Cu. In CsCu_3Cl_5 , however, the strong polar Cu-Cl bonding results in an enhanced crystal field splitting, that separates partially filled valence bonds from fully filled bonding and empty anti-bonding states.

This is directly reflected in the real space arrangement of chlorine atoms around each copper atom, forming a distorted octahedron, elongated by 0.21 Å towards the center of the hexagonal plaquette (see the SM). Within the octahedra, the spatial proximity of the Cu d -orbitals and Cl p -orbitals induces a pronounced splitting in the d -orbital energy levels. Both effects produce a uniquely isolated and undistorted kagome bandstructure close to the Fermi level. In addition, CsCu_3Cl_5 is distinct from related 135 compounds by its inverted band ordering, with the flat band at the bottom (Fig. 1(c)). This sets an m -type vHS in the vicinity of the Fermi level, opposed to the widely studied p -type variant, with important consequences upon the inclusion of interaction effects.

Electronic correlations across kagome compounds The members of the 135 family are generally considered weakly correlated, where phonons play a crucial role in charge ordering mechanism in collaboration or competi-

tion with electronic interactions [25, 26].

To estimate interaction parameters from first principles, we perform constrained random phase approximation (cRPA) calculations [27–30] for pristine CsCu_3Cl_5 (see SM for details and results for the twisted configuration), using as the target space a set of Wannier functions derived from the Wannier model described later in this paper. The resulting screened on-site effective Coulomb interaction is $U = 3.6\text{ eV}$ (bare on-site Coulomb interaction $U_{\text{bare}} = 14.7\text{ eV}$). With the quite narrow bandwidth t , this yields a ratio $U/t \approx 4.7$, placing CsCu_3Cl_5 above the weakly correlated AV_3Sb_5 compounds with $U/t < 1$ [30] and well below the strongly correlated Herbertsmithite in the region of $U_{\text{bare}}/t \approx 20$ [31]. The qualitative findings are consistent with a bond length analysis [32], that estimates the relative degree of correlation across various kagome compounds by the transition metal to ligand distance as explicated in the SM. This classification aligns well with the picture, that a larger filling fraction of the $3d$ shell in copper compared to Ti (d^1) [23], V (d^3) [33] or Cr (d^4) [34] as the central block of the kagome network can enhance local correlations.

A notable exception to this rule is presented by CsCr_3Sb_5 , that displays an admixture of charge and magnetically ordered phases at low temperatures [34, 35]: Opposed to other members of the 135 family, this compound features a flat band in vicinity of the Fermi level [36]. The large spectral weight close to the Fermi level significantly enhances magnetic fluctuations and drives the system to strong coupling irrespective of the U over bandwidth ratio [37–39]. Consequently, not only the bare interaction strength inside the correlated manifold plays a crucial role in determining the degree of correlations in a material. Likewise, the available low-lying states for electronic scattering processes play a decisive role beyond crystal field effects. In particular, pronounced Fermi surface nesting can drive the system to stronger coupling as canonically encountered close to vH filling. In kagome compounds, the non-trivial quantum geometry of the electronic eigenstates around the vHS points adds an additional layer of inference to the estimation of correlation strengths: In V-based 135 kagome compounds, the low lying vHS is of pure p -type, *i.e.* each vHS point is exclusively supported by electronic states on one of the three kagome sublattice sites [10, 11]. This reduces the effectiveness of local Coulomb interactions in driving Fermi surface instability via the celebrated sublattice interference (SI) mechanism [9, 12] with two important corollaries for the AV_3Sb_5 family: Firstly, the enhanced relevance of non-local Coulomb interactions leads to the absence of phases involving local particle-hole pairs at intermediate coupling [40, 41]. Secondly, phonon coupling arising from a delocalized charge density across the sublattices gains significant importance, making it difficult to discern whether the observed instabilities are driven by phonons or electronic correlations [42, 43].

Van Hove scattering at m -type filling In CsCu_3Cl_5 , the much less studied m -type vHS promotes a qualitatively different behavior. The sublattice occupation at the upper van Hove filling of CsCu_3Cl_5 is indicated in Fig. 2(d). At the three inequivalent van Hove points M_γ , the electronic states are equally distributed across two of the three sublattices with vanishing contribution on the third one. This configuration is known as a mixed m -type van Hove singularity [9]. Under scattering with $\mathbf{q} = \text{M}$, the electronic eigenstates at a vHS point transition to states comprised of a different combination of two sublattices. This ensures that one sublattice is occupied both before and after scattering and allows on-site interactions to mediate vHS nesting processes. While this weakens the effect of SI compared to the p -type case, on-site scattering is still partially restricted, as the local Hubbard interaction U acts only on one of the three sublattices at each inequivalent M-point. In the same way the nearest-neighbor (NN) interaction V can mediate scattering between one defined pair of sublattices. Hence, scattering events with the nesting vector M_γ with $M_\alpha = M_\beta + M_\gamma$ between the vH points can be decomposed into a site local and non-local component

$$\begin{aligned} \langle u(M_\alpha) | \langle u(M_\alpha) | \Gamma_{o_1 o_2 o_3 o_4}(M_\gamma) | u(M_\beta) \rangle | u(M_\beta) \rangle \\ = \Gamma_{\gamma\gamma\gamma\gamma}(M_\gamma) + \Gamma_{\alpha\alpha\beta\beta}(M_\gamma) . \end{aligned} \quad (1)$$

Here, $u(M_\alpha)$ is the eigenstate of the non-interacting Hamiltonian at the vH point M_α and Γ the two-particle interaction. Thereby, both interaction scales, U and V , operate at similar scales due to the effect of the partial sublattice polarization of the vH points. This leads to a regime where both local and non-local interactions contribute significantly, and U and V are of comparable importance. Moreover, the m -type vHS corresponds to a more localized electronic structure in momentum space [9, 12, 13]. As a result, electrons couple less efficiently to phonons, suppressing phonon-driven instabilities and making electronic correlations more effective.

The correlation strength within the low energy manifold of CsCu_3Cl_5 is therefore anticipated to reside in a sweet spot between that of the weakly correlated CsV_3Sb_5 , and the strongly correlated Herbertsmithite.

Wannier model The isolated nature of the three characteristic kagome bands allows to capture the electronic structure of CsCu_3Cl_5 around E_F with a single orbital per kagome site. To construct a tight-binding model with maximally localized Wannier functions (MLWF), we begin with an initial approximation using a linear combination of d_{xz} and d_{yz} orbitals. After the spread minimization, three MLWFs are obtained, each centered on a distinct site of the kagome lattice and oriented within the central plane of the coordinating octahedra. These MLWFs share identical shapes, originating from a linear combination of the $d_{x^2-y^2}$ orbital (in the local reference frame of this site) and Cl p -orbitals. Details on the orientations of the local reference frames are provided in

the SM. An example MLWF is illustrated in Fig. 2(a),(b) with the orientation of the corresponding octahedron outlined in gray. $\hat{\mathbf{a}}, \hat{\mathbf{b}}, \hat{\mathbf{c}}$ span the (global) reference frame of the crystal, while $\hat{\mathbf{z}}$ aligns with the octahedron axis. The three MLWFs map onto each other under 60° rotation. These orbitals reflect the B_{2g} elementary band representation of $P6/mmm$, well separated from B_{3g} by the pronounced Jahn-Teller distortion described above [44].

By extracting bands from this three-orbital tight-binding model and comparing them with DFT band calculations in Fig. 2(c), we observe a perfect alignment of the bands, combined with a very small spread. This allows for a description using MLWF, making the three-orbital description a simple and well-suited model for many-body calculations. To study possible instabilities of CsCu_3Cl_5 , we equip the non-interacting theory with two particle interactions. Following the discussion of the preceding section and preceding works on the kagome lattice [12, 13, 41], we choose bare interactions consisting of on-site U and NN repulsion V ,

$$\hat{H}_I = U \sum_{\mathbf{i}} \hat{n}_{\mathbf{i}\uparrow} \hat{n}_{\mathbf{i}\downarrow} + V \sum_{\langle \mathbf{i}, \mathbf{j} \rangle, \sigma \sigma'} \hat{n}_{\mathbf{j}\sigma} \hat{n}_{\mathbf{i}\sigma'}, \quad (2)$$

where $\hat{n}_{\mathbf{j}\sigma} = \hat{c}_{\mathbf{j}\sigma}^\dagger \hat{c}_{\mathbf{j}\sigma}$ is the fermionic number operator on site \mathbf{j} with spin σ . As discussed above, the reduced SI at the m -type vHS - compared to the extensively investigated p -type scenario - allows local and long-range interactions to contribute on a more equal footing. Hence, V cannot be simply neglected as for e.g. done in Ref. [45].

Many-body analysis of magnetic instabilities The small number of bands crossing the Fermi level and the absence of local degrees of freedom in the Wannierized model make it well-suited for exploring the system's ordering tendencies using numerical many-body methods. We perform functional renormalization group (FRG) calculations, utilizing the truncated unity implementation provided by the divERGE code base [46]. The FRG provides a well-defined interpolation from the non-interacting model to a low-energy effective theory near the Fermi level by successively integrating out high-energy degrees of freedom [47, 48]. During this RG flow, all quantum fluctuations involving states outside this restricted manifold are incorporated in the screening of the effective two-particle interaction. This is achieved within the FRG by a perturbative expansion of the possible scattering processes, that allows for an unbiased treatment of symmetry breaking transitions in the superconducting, charge, and magnetic channel. This makes FRG a distinguished method for weak to intermediate coupling strengths, *i.e.* the interaction regime suitable for the exploration of itinerant magnetic orders. Further details on the FRG calculations can be found in the SM.

Our FRG analysis reveals a $2 \times 2 \times 1$ magnetic order depicted in Fig. 3, which can be traced to a collaborative effect of two interaction length scales which

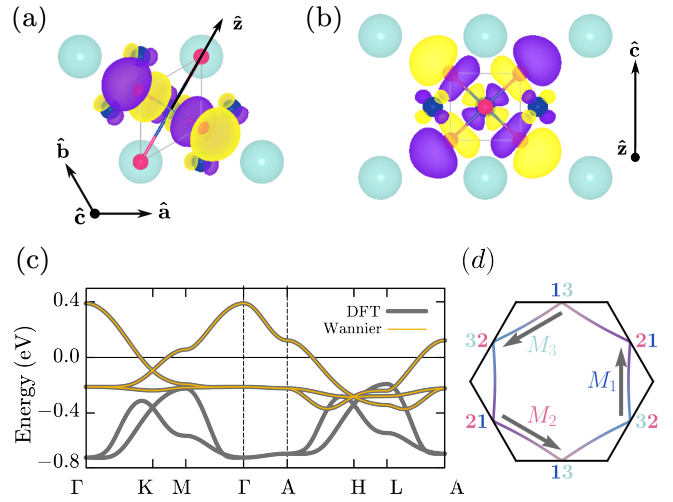


FIG. 2. Wannier orbital centered at the Cu site seen from (a) top and (b) side view of the pristine structure. The site-local reference axis $\hat{\mathbf{z}}$ is pointing towards the center of the hexagonal plaquettes. Purple/yellow orbital lobes indicate the phase of the MLWF. (c) Comparison of the DFT band dispersion (gray) with bands obtained from the Wannier three-orbital tight-binding model (yellow). (d) Fermi surface in the $k_z = 0$ plane for the non-interacting bandstructure at the upper vH filling and dominant nesting vectors. The colors indicate the eigenstate contributions on the three different sublattices. At the three M points, *i.e.* the vH points, the state is equally composed of two sublattices given by the sublattice labels.

operate at equal strength for an m -type vHS. The on-site U favors the formation of local spin polarization to avoid double occupancy on the sublattice site – this leads to long-range antiferromagnetic order at the Fermi surface nesting vector \mathbf{M}_γ on the sublattice sites γ that do not suffer from SI. Meanwhile, NN V promotes the coupling of adjacent sites and generically favors bond orders over local particle-hole pairs, as known from the p -type vHS scenario [9]. This results in a magnetic state $\vec{\Delta}_\gamma = \vec{\Delta}_\gamma^{SDW} + \vec{\Delta}_\gamma^{SBO}$ which combines spin density wave order (SDW)

$$\vec{\Delta}_\gamma^{SDW} \propto \sum_{\mathbf{i}} \cos(\mathbf{i} \cdot \mathbf{M}_\gamma) \langle \hat{c}_{\mathbf{i}\gamma\sigma}^\dagger \vec{\sigma}^{\sigma\sigma'} \hat{c}_{\mathbf{i}\gamma\sigma'} \rangle \quad (3)$$

with finite relative angular momentum components

$$\vec{\Delta}_\gamma^{SBO} \propto \sum_{\langle \mathbf{i}, \mathbf{j} \rangle} \cos(\mathbf{i} \cdot \mathbf{M}_\gamma) \Delta_\gamma^{\mathbf{ij}\alpha\beta} \langle \hat{c}_{\mathbf{i}\alpha\sigma}^\dagger \vec{\sigma}^{\sigma\sigma'} \hat{c}_{\mathbf{j}\beta\sigma'} \rangle, \quad (4)$$

that constitute a spin bond order phase (SBO). Here, $\langle \mathbf{i}, \mathbf{j} \rangle$ is the sum over unit cell vectors \mathbf{i}, \mathbf{j} such that \mathbf{i}, α and \mathbf{j}, β describe neighboring sites, and all doubly occurring indices are summed over. The real space representations of the SBO order parameter $\Delta_\gamma^{\mathbf{ij}\alpha\beta}$ are given in the SM.

At the M -point, the associated little group to the point group $P6/mmm$ is given by mmm , which is equivalent to the local symmetry group of the individual kagome sites on the 3f Wyckoff positions. Consequently, the SDW

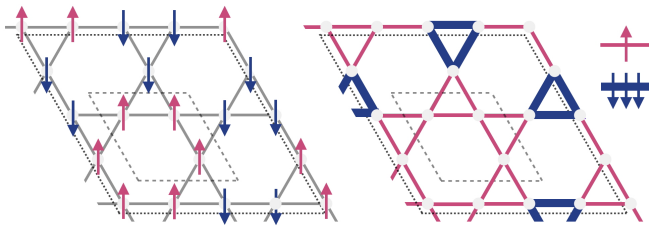


FIG. 3. Magnetic ordering vector of the Cu kagome network as obtained from combined FRG + GL analysis at m -type vH filling. The order parameter blends an collinear antiferromagnetic arrangement of local magnetic moments given in Eq. (3) (left) and NN spin bond terms of Eq. (4) (right) reminiscent of a tri-hexagonal pattern. Here, red/blue denote spin up/down on the indicated sites and bonds along the chosen quantization axis. While the relative strength of on-site ($\vec{\Delta}^{SDW}$) and bond magnetization ($\vec{\Delta}^{SBO}$) is dependent on the interaction parameter, their relative sign is fixed by the many-body analysis. To maintain vanishing net magnetization, the spin polarization on the \downarrow bonds surpasses the value on the \uparrow bonds by a factor of 3, as indicated by the line thickness.

order parameter, which transforms trivially under all elements of mmm , has support only on sublattice γ . In order to mix with the U driven on-site magnetization, the SBO phase transforms within the A_g irreducible representation of mmm and thus represents an extended s -wave magnetization pattern. This is a crucial precondition for the magnetic state to lower its free energy via spin fluctuations of both local and non-local moments present in the m -type vH scenario. Contrarily, the p -type scenario does not allow for a local moment formation at the Fermi level due to SI [9]. While the p -type scenario opens up opportunities for bond-magnetization in non-trivial irreducible representations, it also limits the available free-energy gain, since the spin polarization exhibits strong momentum dependence with additional nodes in the quasi-particle spectrum, that cannot contribute from the dominant on-site repulsion U .

A Ginzburg-Landau (GL) analysis (cf. SM) shows that near the onset of magnetic order, the favoured state is a collinear order in which SDW and SBO point along the same axis (Fig. 3), and modulate with a star-of-David pattern. The magnetic arrangement breaks Z_4 translation and spin rotation symmetries, and transforms within the three-dimensional F_2' irrep of the extended C_{6v}''' symmetry group of the enlarged 2×2 unit cell [49]. While retaining the original $P6/mmm$ symmetry, the superposition of the three different A_g states leads to a triple enhancement of the hexagonal bonds compared to the star-like bonds to ensure vanishing net magnetization. This marks the first instance of spontaneous magnetization in kagome metals driven by quantum fluctuations.

Induced spin current order This change of paradigm - from the local moment-driven, to itinerant magnetism - comes with the promise of more, yet unprecedented phases. At lower temperature, deeper in the symmetry-

broken phase, higher-order terms in GL expansion of the free-energy become important. In this circumstance, the SDW/SBO configuration may cease to be uniaxial, promoting an octahedral spin configuration, which permits a more intriguing coupling of the order parameter to sub-leading magnetic fluctuations via the spin chirality coupling (cf. SM). For charge-ordered phases, the coupling of real and imaginary bond order is known to promote subsidiary loop current orders [40, 50]; here we draw an interesting parallel to magnetic instabilities. Spin currents are even under time-reversal symmetry (TRS). Hence, a coupling to SBO/SDW order can already appear at first-order in the spin-current order (SCO) parameter via the cubic term

$$\mathcal{F}^{(3)} \propto \sum_{\alpha\beta\gamma} \varepsilon_{\alpha\beta\gamma} \vec{\Delta}_\alpha^s \cdot (\vec{\Delta}_\beta^s \times \vec{\Delta}_\gamma^{SCO}) \quad (5)$$

where $s = \{SBO, SDW\}$. Minimizing this contribution to the free energy produces a state in which $\vec{\Delta}_\alpha^s \perp \vec{\Delta}_\beta^s \perp \vec{\Delta}_\gamma^{SCO}$, i.e. the $\vec{\Delta}^s$ vectors at the three M points are mutually perpendicular, and locked parallel to the SCO vector, $\vec{\Delta}_\alpha^s \parallel \vec{\Delta}_\alpha^{SCO}$. This locking between spin and M -point is a kind of “spontaneous spin-orbit coupling”. Eq. (5) is linear in $\vec{\Delta}^{SCO}$, which implies that non collinear $\vec{\Delta}^s$ is expected to immediately induce SCO, and conversely, the presence of SCO can induce canting of the $\vec{\Delta}^s$ state.

This mechanism for the emergence of spin current appears as a direct consequence of cascading phase transitions characteristic of kagome materials [51]. The only instance of spin currents reported to date is in FeGe, in the A-type AFM phase [52–54]. However, in that system the SCO can be simply viewed as loop current formation of spin-polarized electrons [14, 55, 56]. The new mechanism we describe above gives way to uncharted territory of magnetic states due to the unique features of the kagome lattice, combining the effects of geometric frustration and SI in the moderately coupled regime.

Summary This study explores the emergence of itinerant magnetism in kagome lattice systems. Using CsCu_3Cl_5 as theoretical platform, we achieve an electronic structure displaying the three characteristic kagome bands around the Fermi level almost without any interference from additional bands. A description by means of local reference frames enables the identification of a minimal tight-binding model using three maximally localized Wannier orbitals. While many kagome materials exhibit a more complex description, with several vHS near the Fermi level which may interplay to form novel electronic orders [10, 11, 57–60], our exemplary Cu-based kagome material CsCu_3Cl_5 exhibits an isolated m -type vHS close to the Fermi level, providing a model realization of the kagome Hubbard model, worth of exploring in future material science experiments.

Our FRG study reveals a unprecedented unconventional $2 \times 2 \times 1$ antiferromagnetic ordering. While

kagome magnets have attracted much attention in recent years, the formation of long-range magnetization is usually fostered by dipole interactions of localised magnetic moments rather than an intrinsic electronic mechanism which is at display here [16, 61]. In the presented scenario, quantum fluctuations provide the driving force for the magnetic transition. This expands the catalogue of magnetic states on the kagome lattice: We predict a spin bond order phase with descendent spin current patterns on the kagome lattice, featuring a finite relative angular momentum of the spin-1 particle-hole pair in analogy to spin-0 charge bond order patterns. Our analysis marks the first chapter of emergent magnetic order from itinerant electrons on the kagome lattice, and sets magnetic instabilities on the landscape of symmetry-broken phases in metallic kagome compounds.

Acknowledgements We thank S. Enzner, L.M. Schoop, J.B. Profe, and L. Klebl for valuable discussions and feedback on this work. A.W., M.D., H.H. and R.T. are supported by the Deutsche Forschungsgemeinschaft (DFG, German Research Foundation) through Project-ID 258499086 - SFB 1170, through the Würzburg-Dresden Cluster of Excellence on Complexity and Topology in Quantum Matter - ct.qmat Project-ID 390858490 - EXC 2147, and the research unit QUAST, FOR 5249-449872909 (Project 3). A.C. acknowledges support from PNR MUR project PE0000023-NQSTI. M.D. is grateful for support from a PhD scholarship of the Studienstiftung des Deutschen Volkes. A.W., A.C., D.D.S. and R.T. acknowledge the Gauss Centre for Supercomputing e.V. (<https://www.gauss-centre.eu>) for funding this project by providing computing time on the GCS Supercomputer SuperMUC-NG at Leibniz Supercomputing Centre (<https://www.lrz.de>) where the DFT and Wannier-based calculations were performed. M.D., H.H. and R.T. are grateful for HPC resources provided by the Erlangen National High Performance Computing Center (NHR@FAU) of the Friedrich-Alexander-Universität Erlangen-Nürnberg (FAU), that were used for the FRG calculations. NHR funding is provided by federal and Bavarian state authorities. NHR@FAU hardware is partially funded by the DFG - 440719683.

Author contributions R.T. initiated and supervised the project. R.T., A.W., A.C., and F.v.R. designed the model system. A.W., A.C. and D.D.S. conducted the first principles calculations and the related Wannier-based analysis. H.H. and M.D. performed the FRG calculations. M.D. carried out the GL analysis with input from H.D.S. and J.I.. A.W., M.D. and J.I. wrote the manuscript with input from all authors.

* matteo.duerrnagel@uni-wuerzburg.de

† ronny.thomale@uni-wuerzburg.de

- [1] Yu-Xiao Jiang, Jia-Xin Yin, M. Michael Denner, Nana Shumiya, Brenden R. Ortiz, Gang Xu, Zurab Guguchia, Junyi He, Md Shafayat Hossain, Xiaoxiong Liu, Jacob Ruff, Linus Kautzsch, Songtian S. Zhang, Guoqing Chang, Ilya Belopolski, Qi Zhang, Tyler A. Cochran, Daniel Multer, Maksim Litskevich, Zi-Jia Cheng, Xian P. Yang, Ziqiang Wang, Ronny Thomale, Titus Neupert, Stephen D. Wilson, and M. Zahid Hasan, “Unconventional chiral charge order in kagome superconductor KV_3Sb_5 ,” *Nat. Mater.* **20**, 1353–1357 (2021).
- [2] C. Mielke, D. Das, J.-X. Yin, H. Liu, R. Gupta, Y.-X. Jiang, M. Medarde, X. Wu, H. C. Lei, J. Chang, Pengcheng Dai, Q. Si, H. Miao, R. Thomale, T. Neupert, Y. Shi, R. Khasanov, M. Z. Hasan, H. Luetkens, and Z. Guguchia, “Time-reversal symmetry-breaking charge order in a kagome superconductor,” *Nature* **602**, 245–250 (2022).
- [3] Hong Li, Siyu Cheng, Brenden R Ortiz, Hengxin Tan, Dominik Werhahn, Keyu Zeng, Dirk Johrendt, Binghai Yan, Ziqiang Wang, Stephen D Wilson, *et al.*, “Electronic nematicity without charge density waves in titanium-based kagome metal,” *Nature Physics* **19**, 1591–1598 (2023).
- [4] Zhicheng Jiang, Zhengtai Liu, Haiyang Ma, Wei Xia, Zhonghao Liu, Jishan Liu, Soohyun Cho, Yichen Yang, Jianyang Ding, Jiayu Liu, *et al.*, “Flat bands, non-trivial band topology and rotation symmetry breaking in layered kagome-lattice $RbTi_3Bi_5$,” *Nature Communications* **14**, 4892 (2023).
- [5] Pranab Kumar Nag, Rajib Batabyal, Julian Ingham, Noam Morali, Hengxin Tan, Jahyun Koo, Armando Consiglio, Enke Liu, Nurit Avraham, Raquel Queiroz, *et al.*, “Pomeranchuk instability induced by an emergent higher-order van Hove singularity on the distorted kagome surface of $Co_3Sn_2S_2$,” *arXiv preprint arXiv:2410.01994* (2024).
- [6] Yu-Xiao Jiang, Sen Shao, Wei Xia, M Michael Denner, Julian Ingham, Md Shafayat Hossain, Qingzheng Qiu, Xiquan Zheng, Hongyu Chen, Zi-Jia Cheng, *et al.*, “Van Hove annihilation and nematic instability on a kagome lattice,” *Nat. Mater.* **23**, 1214–1221 (2024).
- [7] Yigui Zhong, Shaozhi Li, Hongxiong Liu, Yuyang Dong, Kohei Aido, Yosuke Arai, Haoxiang Li, Weilu Zhang, Youguo Shi, Ziqiang Wang, Shik Shin, H. N. Lee, H. Miao, Takeshi Kondo, and Kozo Okazaki, “Testing electron–phonon coupling for the superconductivity in kagome metal CsV_3Sb_5 ,” *Nat. Commun.* **14**, 1945 (2023).
- [8] Yaofeng Xie, Yongkai Li, Philippe Bourges, Alexandre Ivanov, Zijin Ye, Jia-Xin Yin, M. Zahid Hasan, Aiyun Luo, Yugui Yao, Zhiwei Wang, Gang Xu, and Pengcheng Dai, “Electron-phonon coupling in the charge density wave state of CsV_3Sb_5 ,” *Phys. Rev. B* **105**, L140501 (2022).
- [9] Maximilian L Kiesel and Ronny Thomale, “Sublattice interference in the kagome hubbard model,” *Phys. Rev. B* **86**, 121105 (2012).
- [10] Yong Hu, Xianxin Wu, Brenden R. Ortiz, Sailong Ju, Xinloong Han, Junzhang Ma, Nicholas C. Plumb, Milan Radovic, Ronny Thomale, Stephen D. Wilson, Andreas P. Schnyder, and Ming Shi, “Rich nature of van Hove singularities in kagome superconductor CsV_3Sb_5 ,” *Nat. Commun.* **13**, 2220 (2022).
- [11] Mingu Kang, Shiang Fang, Jeong-Kyu Kim, Brenden R. Ortiz, Sae Hee Ryu, Jimin Kim, Jonggyu Yoo,

- Giorgio Sangiovanni, Domenico Di Sante, Byeong-Gyu Park, Chris Jozwiak, Aaron Bostwick, Eli Rotenberg, Efthimios Kaxiras, Stephen D. Wilson, Jae-Hoon Park, and Riccardo Comin, “Twofold van Hove singularity and origin of charge order in topological kagome superconductor CsV_3Sb_5 ,” *Nat. Phys.* **18**, 301–308 (2022).
- [12] Maximilian L Kiesel, Christian Platt, and Ronny Thomale, “Unconventional fermi surface instabilities in the kagome hubbard model,” *Phys. Rev. Lett.* **110**, 126405 (2013).
- [13] Wan-Sheng Wang, Zheng-Zhao Li, Yuan-Yuan Xiang, and Qiang-Hua Wang, “Competing electronic orders on kagome lattices at van Hove filling,” *Phys. Rev. B* **87**, 115135 (2013).
- [14] Jun Zhan, Hendrik Hohmann, Matteo Dürrnagel, Ruiqing Fu, Sen Zhou, Ziqiang Wang, Ronny Thomale, Xianxin Wu, and Jiangping Hu, “Loop current order on the kagome lattice,” (2024), submitted.
- [15] F Bert, A Olariu, A Zorko, P Mendels, J C Trombe, F Duc, M A de Vries, A Harrison, A D Hillier, J Lord, A Amato, and C Baines, “Frustrated magnetism in the quantum kagome herbertsmithite $\text{ZnCu}_3(\text{OH})_6\text{Cl}_2$ antiferromagnet,” *Journal of Physics: Conference Series* **145**, 012004 (2009).
- [16] M. R. Norman, “Colloquium: Herbertsmithite and the search for the quantum spin liquid,” *Rev. Mod. Phys.* **88**, 041002 (2016).
- [17] John A McGinney, “Cesium tetrachlorocuprate. structure, crystal forces, and charge distribution,” *Journal of the American Chemical Society* **94**, 8406–8413 (1972).
- [18] Albert W Schlueter, Robert A Jacobson, and Robert E Rundle, “A redetermination of the crystal structure of CsCuCl_3 ,” *Inorganic Chemistry* **5**, 277–280 (1966).
- [19] S. Hull and P. Berastegui, “Crystal structures and ionic conductivities of ternary derivatives of the silver and copper monohalides-II: ordered phases within the $(\text{AgX})_x-(\text{MX})_{1-x}$ and $(\text{CuX})_x-(\text{MX})_{1-x}$ ($M = \text{K, Rb and Cs; X} = \text{Cl, Br and I}$) systems,” *Journal of Solid State Chemistry* **177**, 3156–3173 (2004).
- [20] Robert D Shannon, “Revised effective ionic radii and systematic studies of interatomic distances in halides and chalcogenides,” *Foundations of Crystallography* **32**, 751–767 (1976).
- [21] MV Veidis, GH Schreiber, TE Gough, and Gus J Palenik, “Jahn-teller distortions in octahedral copper (II) complexes,” *Journal of the American Chemical Society* **91**, 1859–1860 (1969).
- [22] Dominik Werhahn, Brenden R. Ortiz, Aurland K. Hay, Stephen D. Wilson, Ram Seshadri, and Dirk Johrendt, “The kagomé metals RbTi_3Bi_5 and CsTi_3Bi_5 ,” *Zeitschrift für Naturforschung B* **77**, 757–764 (2022).
- [23] Jiangang Yang, Xinwei Yi, Zhen Zhao, Yuyang Xie, Taimin Miao, Hailan Luo, Hao Chen, Bo Liang, Wenpei Zhu, Yuhan Ye, Jing-Yang You, Bo Gu, Shenjin Zhang, Fengfeng Zhang, Feng Yang, Zhimin Wang, Qinqun Peng, Hanqing Mao, Guodong Liu, Zuyan Xu, Hui Chen, Haitao Yang, Gang Su, Hongjun Gao, Lin Zhao, and X. J. Zhou, “Observation of flat band, Dirac nodal lines and topological surface states in kagome superconductor CsTi_3Bi_5 ,” *Nat. Commun.* **14**, 4089 (2023).
- [24] Chiara Bigi, Matteo Dürrnagel, Lennart Klebl, Armando Consiglio, Ganesh Pokharel, Francois Bertran, Patrick Le Fèvre, Thomas Jaouen, Hulerich C. Tchouekem, Pascal Turban, Alessandro De Vita, Jill A. Miwa, Justin W. Wells, Dongjin Oh, Riccardo Comin, Ronny Thomale, Ilija Zeljkovic, Brenden R. Ortiz, Stephen D. Wilson, Giorgio Sangiovanni, Federico Mazzola, and Domenico Di Sante, “Pomeranchuk instability from electronic correlations in cst_3bi_5 kagome metal,” (2024), [arXiv:2410.22929](https://arxiv.org/abs/2410.22929) [cond-mat.str-el].
- [25] Brenden R. Ortiz, Samuel M. L. Teicher, Linus Kautzsch, Paul M. Sarte, Noah Ratcliff, John Harter, Jacob P. C. Ruff, Ram Seshadri, and Stephen D. Wilson, “Fermi surface mapping and the nature of charge-density-wave order in the kagome superconductor csv_3sb_5 ,” *Phys. Rev. X* **11**, 041030 (2021).
- [26] Ge He, Leander Peis, Emma Frances Cuddy, Zhen Zhao, Dong Li, Yuhang Zhang, Romona Stumberger, Brian Moritz, Haitao Yang, Hongjun Gao, Thomas Peter Devereaux, and Rudi Hackl, “Anharmonic strong-coupling effects at the origin of the charge density wave in CsV_3Sb_5 ,” *Nat. Commun.* **15**, 1895 (2024).
- [27] F. Aryasetiawan, M. Imada, A. Georges, G. Kotliar, S. Biermann, and A. I. Lichtenstein, “Frequency-dependent local interactions and low-energy effective models from electronic structure calculations,” *Phys. Rev. B* **70**, 195104 (2004).
- [28] Takashi Miyake, Ferdi Aryasetiawan, and Masatoshi Imada, “Ab initio procedure for constructing effective models of correlated materials with entangled band structure,” *Phys. Rev. B* **80**, 155134 (2009).
- [29] Loïc Vaugier, Hong Jiang, and Silke Biermann, “Hubbard u and hund exchange j in transition metal oxides: Screening versus localization trends from constrained random phase approximation,” *Phys. Rev. B* **86**, 165105 (2012).
- [30] Domenico Di Sante, Bongjae Kim, Werner Hanke, Tim Wehling, Cesare Franchini, Ronny Thomale, and Giorgio Sangiovanni, “Electronic correlations and universal long-range scaling in kagome metals,” *Phys. Rev. Res.* **5**, L012008 (2023).
- [31] I. I. Mazin, Harald O. Jeschke, Frank Lechermann, Hunpyo Lee, Mario Fink, Ronny Thomale, and Roser Valentí, “Theoretical prediction of a strongly correlated Dirac metal,” *Nat. Commun.* **5**, 4261 (2014).
- [32] Milena Jovanovic and Leslie M Schoop, “Simple chemical rules for predicting band structures of kagome materials,” *Journal of the American Chemical Society* **144**, 10978–10991 (2022).
- [33] Brenden R. Ortiz, Samuel M. L. Teicher, Yong Hu, Julia L. Zuo, Paul M. Sarte, Emily C. Schueller, A. M. Milinda Abeykoon, Matthew J. Krogstad, Stephan Rosenkranz, Raymond Osborn, Ram Seshadri, Leon Balents, Junfeng He, and Stephen D. Wilson, “ CsV_3Sb_5 : A \mathbb{Z}_2 topological kagome metal with a superconducting ground state,” *Phys. Rev. Lett.* **125**, 247002 (2020).
- [34] Yi Liu, Zi-Yi Liu, Jin-Ke Bao, Peng-Tao Yang, Liang-Wen Ji, Si-Qi Wu, Qin-Xin Shen, Jun Luo, Jie Yang, Ji-Yong Liu, Chen-Chao Xu, Wu-Zhang Yang, Wan-Li Chai, Jia-Yi Lu, Chang-Chao Liu, Bo-Sen Wang, Hao Jiang, Qian Tao, Zhi Ren, Xiao-Feng Xu, Chao Cao, Zhu-An Xu, Rui Zhou, Jin-Guang Cheng, and Guang-Han Cao, “Superconductivity under pressure in a chromium-based kagome metal,” *Nature* **632**, 1032–1037 (2024).
- [35] Giorgio Sangiovanni, “Superconductor surprises with strongly interacting electrons,” *Nature* **632**, 988–989 (2024).

- [36] Yidian Li, Yi Liu, Xian Du, Siqi Wu, Wenxuan Zhao, Kaiyi Zhai, Yinqi Hu, Senyao Zhang, Houke Chen, Jieyi Liu, Yiheng Yang, Cheng Peng, Makoto Hashimoto, Donghui Lu, Zhongkai Liu, Yilin Wang, Yulin Chen, Guanghan Cao, and Lexian Yang, “Electron correlation and incipient flat bands in the kagome superconductor cscr3sb5 ,” *Nature Communications* **16**, 3229 (2025).
- [37] Siqi Wu, Chenchao Xu, Xiaoqun Wang, Hai-Qing Lin, Chao Cao, and Guang-Han Cao, “Flat-band enhanced antiferromagnetic fluctuations and superconductivity in pressurized cscr3sb5 ,” *Nature Communications* **16**, 1375 (2025).
- [38] Fang Xie, Yuan Fang, Ying Li, Yuefei Huang, Lei Chen, Chandan Setty, Shouvik Sur, Boris Yakobson, Roser Valentí, and Qimiao Si, “Electron correlations in the kagome flat band metal cscr3sb5 ,” *Phys. Rev. Res.* **7**, L022061 (2025).
- [39] Yilin Wang, “Heavy fermions in frustrated hund’s metal with portions of incipient flat bands,” *Phys. Rev. B* **111**, 035127 (2025).
- [40] M. Michael Denner, Ronny Thomale, and Titus Neupert, “Analysis of charge order in the kagome metal AV_3Sb_5 ($A = \text{K, Rb, Cs}$),” *Phys. Rev. Lett.* **127**, 217601 (2021).
- [41] Jonas B. Profe, Lennart Klebl, Francesco Grandi, Hendrik Hohmann, Matteo Dürnagel, Tilman Schwemmer, Ronny Thomale, and Dante M. Kennes, “The kagome hubbard model from a functional renormalization group perspective,” (2024), [arXiv:2402.11916 \[cond-mat.str-el\]](https://arxiv.org/abs/2402.11916).
- [42] Yaojia Wang, Heng Wu, Gregory T McCandless, Julia Y Chan, and Mazhar N Ali, “Quantum states and intertwining phases in kagome materials,” *Nature Reviews Physics* **5**, 635–658 (2023).
- [43] Stefan Enzner, Jan Berges, Arne Schobert, Dongjin Oh, Mingu Kang, Riccardo Comin, Ronny Thomale, Tim O. Wehling, Domenico Di Sante, and Giorgio Sangiovanni, “Phonon fluctuation diagnostics: Origin of charge order in av3sb5 kagome metals,” (2025), [arXiv:2504.07883 \[cond-mat.str-el\]](https://arxiv.org/abs/2504.07883).
- [44] Xianxin Wu, Tilman Schwemmer, Tobias Müller, Armando Consiglio, Giorgio Sangiovanni, Domenico Di Sante, Yasir Iqbal, Werner Hanke, Andreas P Schnyder, M Michael Denner, *et al.*, *Phys. Rev. Lett.* **127**, 177001 (2021).
- [45] Qing-Geng Yang, Meng Yao, Da Wang, and Qiang-Hua Wang, “Charge bond order and s -wave superconductivity in the kagome lattice with electron-phonon coupling and electron-electron interaction,” *Phys. Rev. B* **109**, 075130 (2024).
- [46] Jonas B. Profe, Dante M. Kennes, and Lennart Klebl, “divERGE implements various Exact Renormalization Group examples,” *SciPost Phys. Codebases*, 26 (2024).
- [47] Walter Metzner, Manfred Salmhofer, Carsten Honerkamp, Volker Meden, and Kurt Schönhammer, “Functional renormalization group approach to correlated fermion systems,” *Rev. Mod. Phys.* **84**, 299–352 (2012).
- [48] C. Platt, W. Hanke, and R. Thomale, “Functional renormalization group for multi-orbital fermi surface instabilities,” *Advances in Physics* **62**, 453–562 (2013).
- [49] J. W. F. Venderbos, “Symmetry analysis of translational symmetry broken density waves: Application to hexagonal lattices in two dimensions,” *Phys. Rev. B* **93**, 115107 (2016).
- [50] Chunyu Guo, Glenn Wagner, Carsten Putzke, Dong Chen, Kaize Wang, Ling Zhang, Martin Gutierrez-Amigo, Ion Errea, Maia G. Vergniory, Claudia Felser, Mark H. Fischer, Titus Neupert, and Philip J. W. Moll, “Correlated order at the tipping point in the kagome metal CsV_3Sb_5 ,” *Nat. Phys.* **20**, 579–584 (2024).
- [51] He Zhao, Hong Li, Brenden R. Ortiz, Samuel M. L. Teicher, Takamori Park, Mengxing Ye, Ziqiang Wang, Leon Balents, Stephen D. Wilson, and Ilija Zeljkovic, “Cascade of correlated electron states in the kagome superconductor CsV_3Sb_5 ,” *Nature* **599**, 216–221 (2021).
- [52] Jia-Xin Yin, Yu-Xiao Jiang, Xiaokun Teng, Md. Shafayat Hossain, Sougata Mardanya, Tay-Rong Chang, Zijin Ye, Gang Xu, M. Michael Denner, Titus Neupert, Benjamin Lienhard, Han-Bin Deng, Chandan Setty, Qimiao Si, Guoqing Chang, Zurab Guguchia, Bin Gao, Nana Shumiya, Qi Zhang, Tyler A. Cochran, Daniel Multer, Ming Yi, Pengcheng Dai, and M. Zahid Hasan, “Discovery of charge order and corresponding edge state in kagome magnet FeGe ,” *Phys. Rev. Lett.* **129**, 166401 (2022).
- [53] Xiaokun Teng, Lebing Chen, Feng Ye, Elliott Rosenberg, Zhaoyu Liu, Jia-Xin Yin, Yu-Xiao Jiang, Ji Seop Oh, M. Zahid Hasan, Kelly J. Neubauer, Bin Gao, Yaofeng Xie, Makoto Hashimoto, Donghui Lu, Chris Jozwiak, Aaron Bostwick, Eli Rotenberg, Robert J. Birgeneau, Jiun-Haw Chu, Ming Yi, and Pengcheng Dai, “Discovery of charge density wave in a kagome lattice antiferromagnet,” *Nature* **609**, 490–495 (2022).
- [54] Xiaokun Teng, Ji Seop Oh, Hengxin Tan, Lebing Chen, Jianwei Huang, Bin Gao, Jia-Xin Yin, Jiun-Haw Chu, Makoto Hashimoto, Donghui Lu, Chris Jozwiak, Aaron Bostwick, Eli Rotenberg, Garrett E. Granroth, Binghai Yan, Robert J. Birgeneau, Pengcheng Dai, and Ming Yi, “Magnetism and charge density wave order in kagome FeGe ,” *Nat. Phys.* **19**, 814–822 (2023).
- [55] Shulun Han, Linyang Li, Chi Sin Tang, Qi Wang, Lingfeng Zhang, Caozheng Diao, Mingwen Zhao, Shuo Sun, Lijun Tian, Mark B. H. Breese, Chuanbing Cai, Milorad V. Milosevic, Yanpeng Qi, Andrew T. S. Wee, and Xinmao Yin, “Orbital origin of magnetic moment enhancement induced by charge density wave in kagome FeGe ,” (2024), [arXiv:2407.01076 \[cond-mat.str-el\]](https://arxiv.org/abs/2407.01076).
- [56] Xiaokun Teng, David W. Tam, Lebing Chen, Hengxin Tan, Yaofeng Xie, Bin Gao, Garrett E. Granroth, Alexandre Ivanov, Philippe Bourges, Binghai Yan, Ming Yi, and Pengcheng Dai, “Spin-charge-lattice coupling across the charge density wave transition in a kagome lattice antiferromagnet,” (2024), [arXiv:2404.04459 \[cond-mat.str-el\]](https://arxiv.org/abs/2404.04459).
- [57] Xianxin Wu, Tilman Schwemmer, Tobias Müller, Armando Consiglio, Giorgio Sangiovanni, Domenico Di Sante, Yasir Iqbal, Werner Hanke, Andreas P. Schnyder, M. Michael Denner, Mark H. Fischer, Titus Neupert, and Ronny Thomale, “Nature of unconventional pairing in the kagome superconductors AV_3Sb_5 ($A = \text{K, Rb, Cs}$),” *Phys. Rev. Lett.* **127**, 177001 (2021).
- [58] Heqiu Li, Yong Baek Kim, and Hae-Young Kee, “Intertwined van Hove singularities as a mechanism for loop current order in kagome metals,” *Phys. Rev. Lett.* **132**, 146501 (2024).
- [59] Harley D. Scammell, Julian Ingham, Tommy Li, and Oleg P Sushkov, “Chiral excitonic order from twofold van hove singularities in kagome metals,” *Nat. Commun.* **14**, 605 (2023).
- [60] Julian Ingham, Armando Consiglio, Domenico di Sante, Ronny Thomale, and Harley D. Scammell, “Theory

- of excitonic order in $\text{scv}_{16}\text{sn}_{16}$,” *arXiv preprint arXiv:2410.16365* (2024).
- [61] Jia-Xin Yin, Biao Lian, and M. Zahid Hasan, “Topological kagome magnets and superconductors,” *Nature* **612**, 647–657 (2022).
- [62] Mark J. Winter, “Webelements: The periodic table on the www,” <https://winter.group.shef.ac.uk/webelements/chlorine/electronegativity.html>, accessed: 16.12.23.
- [63] S V Streltsov and D I Khomskii, “Orbital physics in transition metal compounds: new trends,” *Physics-Uspekhi* **60**, 1121 (2017).
- [64] Armando Consiglio, Tilman Schwemmer, Xianxin Wu, Werner Hanke, Titus Neupert, Ronny Thomale, Giorgio Sangiovanni, and Domenico Di Sante, “Van Hove tuning of AV_3Sb_5 kagome metals under pressure and strain,” *Phys. Rev. B* **105**, 165146 (2022).
- [65] Harrison LaBollita and Antia S. Botana, “Tuning the van Hove singularities in AV_3Sb_5 ($A = \text{K, Rb, Cs}$) via pressure and doping,” *Phys. Rev. B* **104**, 205129 (2021).
- [66] Chun Lin, Armando Consiglio, Ola Kenji Forslund, Julia Kuspert, M. Michael Denner, Hechang Lei, Alex Louat, Matthew D. Watson, Timur K. Kim, Cephise Cacho, Dina Carbone, Mats Leandersson, Craig Polley, Thiagarajan Balasubramanian, Domenico Di Sante, Ronny Thomale, Zurab Guguchia, Giorgio Sangiovanni, Titus Neupert, and Johan Chang, “Giant strain response of charge modulation and singularity in a kagome superconductor,” (2024), [arXiv:2402.16089](https://arxiv.org/abs/2402.16089) [cond-mat.mtrl-sci].
- [67] Manuel Tuniz, Armando Consiglio, Ganesh Pokharel, Fulvio Parmigiani, Titus Neupert, Ronny Thomale, Giorgio Sangiovanni, Stephen D. Wilson, Ivana Vobornik, Federico Salvador, Federico Cilento, Domenico Di Sante, and Federico Mazzola, “Strain-induced enhancement of the charge-density-wave in the kagome metal SeV_6Sn_6 ,” (2024), [arXiv:2403.18046](https://arxiv.org/abs/2403.18046) [cond-mat.str-el].
- [68] Luigi Ranalli, Carla Verdi, Lorenzo Monacelli, Georg Kresse, Matteo Calandra, and Cesare Franchini, “Temperature-dependent anharmonic phonons in quantum paraelectric ktao_3 by first principles and machine-learned force fields,” *Advanced Quantum Technologies* **6** (2023), 10.1002/qute.202200131.
- [69] G. Kresse and D. Joubert, “From ultrasoft pseudopotentials to the projector augmented-wave method,” *Phys. Rev. B* **59**, 1758–1775 (1999).
- [70] G. Kresse and J. Furthmüller, “Efficient iterative schemes for ab initio total-energy calculations using a plane-wave basis set,” *Phys. Rev. B* **54**, 11169–11186 (1996).
- [71] John P. Perdew, Kieron Burke, and Matthias Ernzerhof, “Generalized gradient approximation made simple,” *Phys. Rev. Lett.* **77**, 3865–3868 (1996).
- [72] Vei Wang, Nan Xu, Jin-Cheng Liu, Gang Tang, and Wen-Tong Geng, “Vasppkit: A user-friendly interface facilitating high-throughput computing and analysis using vasp code,” *Computer Physics Communications* **267**, 108033 (2021).
- [73] Koichi Momma and Fujio Izumi, “Vesta: a three-dimensional visualization system for electronic and structural analysis,” *Journal of Applied Crystallography* **41**, 653–658 (2008).
- [74] Arash A. Mostofi, Jonathan R. Yates, Young-Su Lee, Ivo Souza, David Vanderbilt, and Nicola Marzari, “wannier90: A tool for obtaining maximally-localised wannier functions,” *Computer Physics Communications* **178**, 685–699 (2008).
- [75] “The calculation data are accessible on zenodo under <https://doi.org/10.5281/zenodo.17483257>.”
- [76] Merzuk Kaltak, *Merging GW with DMFT*, Ph.D. thesis, Universität Wien (2015).
- [77] Carsten Honerkamp, “Effective interactions in multiband systems from constrained summations,” *Phys. Rev. B* **85**, 195129 (2012).
- [78] Jonas B. Profe, Jakša Vučičević, P. Peter Stavropoulos, Malte Rösner, Roser Valentí, and Lennart Klebl, “Exact downfolding and its perturbative approximation,” (2025), [arXiv:2507.16916](https://arxiv.org/abs/2507.16916) [cond-mat.str-el].
- [79] Merzuk Kaltak, Alexander Hampel, Martin Schlipf, Indukuru Ramesh Reddy, Bongae Kim, and Georg Kresse, “Constrained random phase approximation: the spectral method,” (2025), [arXiv:2508.15368](https://arxiv.org/abs/2508.15368) [cond-mat.str-el].
- [80] J. Lichtenstein, D. Sánchez de la Peña, D. Rohe, E. Di Napoli, C. Honerkamp, and S.A. Maier, “High-performance functional renormalization group calculations for interacting fermions,” *Computer Physics Communications* **213**, 100–110 (2017).
- [81] Jacob Beyer, Jonas B. Profe, and Lennart Klebl, “Reference results for the momentum space functional renormalization group,” *The European Physical Journal B* **95** (2022), 10.1140/epjb/s10051-022-00323-y.
- [82] Jonas B. Profe and Dante M. Kennes, “ Tu^2frg : a scalable approach for truncated unity functional renormalization group in generic fermionic models,” *The European Physical Journal B* **95**, 60 (2022).
- [83] Takamori Park, Mengxing Ye, and Leon Balents, “Electronic instabilities of kagome metals: Saddle points and Landau theory,” *Phys. Rev. B* **104**, 035142 (2021).
- [84] Rahul Nandkishore, Gia-Wei Chern, and Andrey V. Chubukov, “Itinerant half-metal spin-density-wave state on the hexagonal lattice,” *Phys. Rev. Lett.* **108**, 227204 (2012).
- [85] Chenchao Xu, Siqi Wu, Guo-Xiang Zhi, Guanghan Cao, Jianhui Dai, Chao Cao, Xiaoqun Wang, and Hai-Qing Lin, “Frustrated altermagnetism and charge density wave in kagome superconductor CsCr_3Sb_5 ,” (2023), [arXiv:2309.14812](https://arxiv.org/abs/2309.14812) [cond-mat.supr-con].
- [86] L. Messio, C. Lhuillier, and G. Misguich, “Lattice symmetries and regular magnetic orders in classical frustrated antiferromagnets,” *Phys. Rev. B* **83**, 184401 (2011).

Supplementary Material for Theory of unconventional magnetism in a Cu-based kagome metal

Anja Wenger,¹ Armando Consiglio,² Hendrik Hohmann,¹ Matteo Dürrnagel,^{1,3,*} Fabian O. von Rohr,⁴ Harley D. Scammell,⁵ Julian Ingham,⁶ Domenico Di Sante,⁷ and Ronny Thomale^{1,†}

¹*Institut für Theoretische Physik und Astrophysik and Würzburg-Dresden Cluster of Excellence ct.qmat, Universität Würzburg, 97074 Würzburg, Germany*

²*Istituto Officina dei Materiali, Consiglio Nazionale delle Ricerche, Trieste I-34149, Italy*

³*Institute for Theoretical Physics, ETH Zürich, 8093 Zürich, Switzerland*

⁴*Department of Quantum Matter Physics, University of Geneva, CH-1211 Geneva, Switzerland*

⁵*School of Mathematical and Physical Sciences, University of Technology Sydney, Ultimo, NSW 2007, Australia*

⁶*Department of Physics, Columbia University, New York, NY, 10027, USA*

⁷*Department of Physics and Astronomy, University of Bologna, 40127 Bologna, Italy*

(Dated: November 6, 2025)

CONTENTS

Crystal Structure	S1
Charge Distribution	S1
Local Frame of Reference	S2
Structure-Correlation Link in Kagome Materials	S2
Crystal Distortions and their Stability	S2
Twisted Configuration	S3
Breathing Configuration	S3
Phonon Analysis	S4
Wannier Model of twisted CsCu₃Cl₅	S4
Computational Methods	S5
Density Functional Theory	S5
Constrained Random Phase Approximation	S5
Functional Renormalization Group	S5
Ginzburg-Landau Analysis of the 3Q Order	S6
Emergence of Octahedral Order inside the Collinear Magnetic Phase	S8
The Role of the \mathbf{k}_z-Dispersion	S8

CRYSTAL STRUCTURE

The unit cell of CsCu₃Cl₅ is defined by the vectors

$$\hat{\mathbf{a}} = (6.025, 0.000, 0.000)$$

$$\hat{\mathbf{b}} = (-3.013, 5.218, 0.000)$$

$$\hat{\mathbf{c}} = (0.000, 0.000, 7.027).$$

Pristine CsCu₃Cl₅ is configured in a $P6/mmm$ space group, with atomic positions specified in fractional coordinates relative to these vectors listed in Tab. SI.

Atom	a	b	c
Cs1	0.000	0.000	0.000
Cu1	0.500	0.500	0.500
Cu2	0.500	0.000	0.500
Cu3	0.000	0.500	0.500
Cl1	0.000	0.000	0.500
Cl2	0.667	0.333	0.736
Cl3	0.333	0.667	0.264
Cl4	0.333	0.667	0.736
Cl5	0.667	0.333	0.264

TABLE SI. Atomic positions of pristine CsCu₃Cl₅ in direct coordinates.

CHARGE DISTRIBUTION

To examine the charge distribution within the CsCu₃Cl₅ compound, we must examine the oxidation states of the involved elements. Utilizing the Pauling scale, which spans from 3.98 (fluorine, the most electronegative) to 0.7 (francium, the least electronegative), we find that Cs, with an electronegativity of 0.79, typically adopts an oxidation state of +1 in compounds. Conversely, Cl, having an electronegativity of 3.16, predominantly exists in a -1 oxidation state. The transition metal copper, with an electronegativity of 1.9, commonly exhibits oxidation states of +2 and, less common, +1 or +3 [62]. To determine the formal (integer) charges of the atoms in CsCu₃Cl₅, we distribute (integer) electrons among the unit cell ions to achieve an overall neutral compound. The $6s^1$ electron in cesium is readily relinquished due to its weak binding. Chlorine, requiring only one electron to complete its $3p^6$ configuration, strongly attracts electrons. As a result, we draw four electrons from the three copper atoms. Applying integer charges, two of the Cu atoms are in the less common +1 state, while one is in the +2 state. Given the $P6/mmm$ symmetry of the compound, the choice of which copper atom assumes the +2 state is equivalent, as they can be transformed into each other through a simple 120° rotation. With three energetically

equivalent possibilities for charge distribution, a Lewis resonance can emerge, allowing electrons to hop between the Cu+1 and Cu+2 sites with equal probability. This resonance creates three Cu+2 sites, with two electrons uniformly hopping between them, resulting in a uniform distribution of $-2/3$ per copper site. Consequently, each Cu has an effective charge of $+4/3$. To assess the stability of this charge distribution, an initial magnetic moment imbalance among the Cu atoms is intentionally introduced, followed by relaxation of the electronic degrees of freedom. The outcome consistently reflects the same uniform charge distribution. This suggests that the uniform configuration is not a mere consequence of symmetric initial parameters in the calculations, but rather a stable configuration imposed by the inherent symmetry of the system.

LOCAL FRAME OF REFERENCE

Fig. S1 visualizes the unit cell's three copper atoms (Cu1, Cu2, Cu3) and the orientations of their distorted Cl octahedra within the crystal. The elongated side of the Cl octahedron aligns along $\hat{\mathbf{a}} + \hat{\mathbf{b}}$ for Cu1, $\hat{\mathbf{a}}$ for Cu2, and $\hat{\mathbf{b}}$ for Cu3. We chose a local reference frame for each octahedra such that the elongation observed in pristine CsCu_3Cl_5 is oriented along the $\hat{\mathbf{z}}$ -direction, visualized in Fig. S1 (right). Each octahedron's local reference frame has the Cu atom at the origin, with $\hat{\mathbf{z}}$ along the elongated tips and $\hat{\mathbf{x}}, \hat{\mathbf{y}}$ towards the corners.

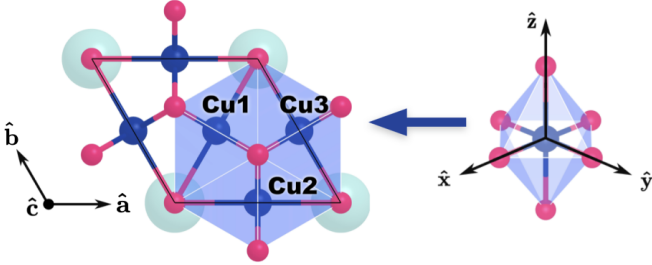


FIG. S1. Top view of the kagome plane (left) highlighting the three copper atoms with the local reference frame around each Cu atom (right).

STRUCTURE-CORRELATION LINK IN KAGOME MATERIALS

To estimate the expected interaction regime for the low energy manifold of CsCu_3Cl_5 , we follow the procedure outlined in Ref. [32]: the degree of electronic correlations in kagome compounds can be understood based on the relative distances between the transition metal atoms, responsible for the electron hopping, and the surrounding

ligands, which influence the strength of the crystal field and ligand hybridization.

In weakly correlated CsV_3Sb_5 , the V atoms are coordinated by nearly undistorted Sb-octahedra with a bond length ratio between neighboring kagome sites ($d(\text{V-V}) = 2.75 \text{ \AA}$) and V-ligand distance ($d(\text{V-Sb}) = 2.75 \text{ \AA}$) of 1.00. This equal distance between V atoms and their surrounding ligands facilitates significant electron hopping between V sites, leading to more delocalized electrons and weaker correlations.

In the strongly correlated Herbertsmithite, each Cu atom is surrounded by a highly distorted octahedron, with four oxygen atoms playing the dominant role in coordination and two Cl atoms contributing less significantly. The distance between neighbouring kagome sites is $d(\text{Cu-Cu}) = 3.53 \text{ \AA}$ while the nearest Cu-ligand distance is $d(\text{Cu-O}) = 1.99 \text{ \AA}$, giving a bond length ratio of 1.77. Chlorine atoms also bond to copper, but at a greater distance of $d(\text{Cu-Cl}) = 2.99 \text{ \AA}$. The close proximity of the oxygen atoms leads to strong Cu-O bonds that confine the electrons, resulting in significant localization. The large Cu-Cu distance weakens electron hopping between kagome sites, while the strong interaction with oxygen atoms further enhances electron localization, driving Herbertsmithite deep into the Mott-insulating regime with strong electronic correlations.

CsCu_3Cl_5 falls between these two cases. The Cu atoms are coordinated by distorted Cl-octahedra, in the with four equally long bonds out of the kagome plane and two longer bonds in-plane for the pristine case. The Cu-Cu distance is $d(\text{Cu-Cu}) = 3.01 \text{ \AA}$, and the nearest Cu-ligand distance is $d(\text{Cu-Cl}) = 2.40 \text{ \AA}$, giving a bond length ratio of 1.25. This intermediate coordination environment suggests that CsCu_3Cl_5 is likely to exhibit moderate electron correlation. The Cu-Cu distance is longer than in CsV_3Sb_5 but shorter than in Herbertsmithite, allowing for some electron delocalization. At the same time, the weaker Cu-Cl hybridization, compared to the Cu-O bonds in Herbertsmithite, results in reduced electron-electron interactions. This positions CsCu_3Cl_5 between the weakly correlated metallic state of CsV_3Sb_5 and the strongly correlated Mott-insulating state of Herbertsmithite, making it a promising candidate for hosting both itinerant and localized magnetic phenomena.

CRYSTAL DISTORTIONS AND THEIR STABILITY

The complex interplay between electronic structure, orbital ordering and structural dynamics becomes noticeable when analyzing the different structural distortions compatible with the phonon modes of the pristine kagome lattice. This interplay leads indeed to an energy loss known as the Jahn-Teller (JT) effect. The sequence

of events remains still uncertain, whether the JT distortion precedes orbital ordering or vice versa [63]. The focus here lies on the breathing and twisted configurations descending from the pristine structure. Fig. S2 illustrates the evolution of the total energy as a function of the geometry, interpolated at constant volume between the pristine and the two distorted cases. The twisted state is the energetically preferred one by ~ 100 meV per unit cell with respect to the breathing lattice, and by ~ 150 meV per unit cell with respect to the pristine lattice. Finally, we observe that a consistent conclusion is drawn from the analysis of the total free energy F of the three configurations, as a function of an isotropic volume variation, shown in Fig. S2. The twisted case remains the most favourable configuration at least in a $[-5\%, 5\%]$ range around the equilibrium volume, above which a competition with the other phases can be observed. This fact suggests both hydro-static pressure, as well as uni-axial strain, as valid methods for structural and electronic tuning [64–67], whose detailed treatment is beyond the scope of the present work.

Twisted Configuration

Within the twisted kagome configuration, taken as an example, the JT distortion leads to a displacement of the Cu atoms as depicted in Fig. S3(a). Consequently their orbitals become more spatially separated, leading to a reduction in Coulomb repulsion and hybridization and a corresponding decrease in energy. The unit cell's top-view reveals that the Cl ions are still positioned at the center of the Cu triangles, albeit in a twisted

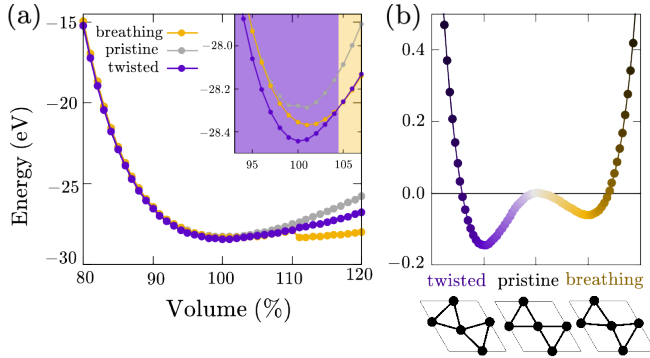


FIG. S2. Energy profiles of the pristine, breathing and twisted configurations for different interpolating geometries and unit cell's sizes. (a) Total free energy as a function of an isotropic change of volume, for all three discussed configurations. The twisted configuration is the most favourable one in a wide range of volume variations. (b) For a unit cell with constant volume, the energy is plotted across varying degrees of interpolation between the pristine and breathing cases, as well as between the pristine and the twisted ones. The twisted configuration stands out as the most energetically favourable.

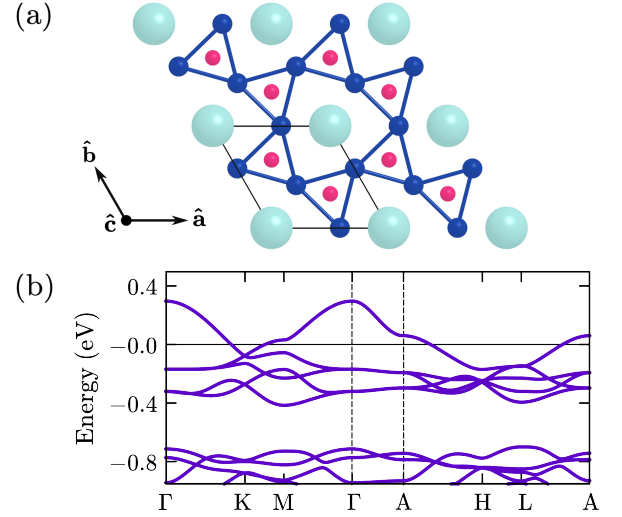


FIG. S3. Twisted configuration of CsCu₃Cl₅. (a) Top view on the crystal with the Cu kagome lattice highlighted by blue lines. Turquoise, blue and pink spheres represent Cs, Cu and Cl atoms. The unit cell is indicated by black lines. (b) Electronic band structure exhibiting a narrower band width and a closer proximity of the m -type vHS to the Fermi level, in contrast to the pristine configuration.

triangular arrangement that reduces the number of symmetries. Comparing the band structure of the twisted configuration shown in Fig. S3(b) with the pristine counterpart, the electronic structure of the former demonstrates a reduced dispersion and a slightly lower energy profile. Additionally, the flat band itself exhibits an increased dispersion due to a reduced destructive interference process among the orbitals of Cu atoms. The Fermi level lies even closer to the (unaffected) m -type vHS than in the pristine case. Given the minimal shift in dispersion, the electronic structure of the twisted configuration remains remarkably close to that of the pristine configuration.

Breathing Configuration

Another structural distortion compatible with the system's phonon modes is the breathing configuration, depicted in Fig. S4(a). The energy of this breathing kagome lattice is lower than the pristine lattice, yet higher than the twisted counterpart. The central observation is a deviation from the previous triangular arrangement, with Cl ions no longer positioned in the center of the Cu triangles. Half of the triangles now possess two long sides and one short side, while the other half exhibit two short sides and one long side. Despite the distortion exhibiting a lower deviation compared to the twisted kagome lattice, it results in an additional reduction in symmetry. As the mirror symmetry is broken, the Dirac cones are

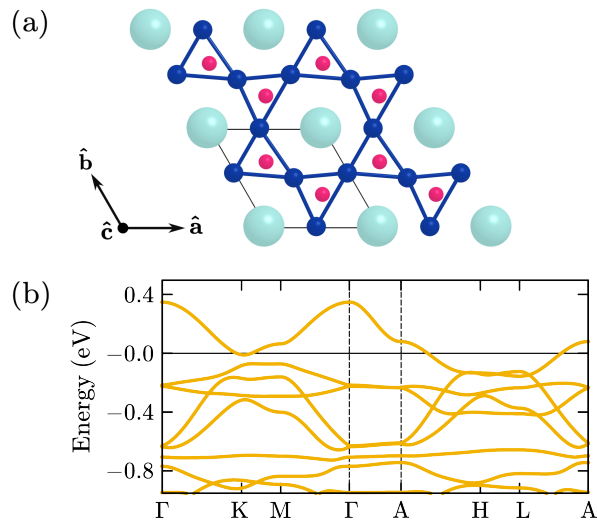


FIG. S4. Breathing configuration of CsCu_3Cl_5 . (a) Top view with the kagome lattice highlighted by blue lines. Turquoise, blue and pink spheres represent Cs, Cu and Cl atoms. The unit cell is indicated by black lines. (b) Electronic band structure of breathing CsCu_3Cl_5 . As the mirror symmetry is broken, the Dirac cone gaps out; the m -type vHS stays close to the Fermi level.

no longer preserved and gap out whereas the m -type vHS still remains in the vicinity of the Fermi level.

Phonon Analysis

A conclusive assessment of compound stability and synthetization of CsCu_3Cl_5 can not be drawn from a purely *ab initio* perspective and consequently lies beyond the scope of our work and methodology. It is well known that DFT can produce unreliable predictions concerning a material's stability due to approximations involved in the derivation of the phonon spectra. For instance, KTaO_3 is a material where DFT incorrectly predicts instability due to imaginary phonon modes. However, when anharmonic effects are included, the phonon spectrum becomes stable [68]. Additionally, even in the presence of imaginary phonon modes the system might be still stable at ambient conditions and eventually exhibit a phonon driven symmetry breaking only at low temperatures. This is a common feature in comparable 135 kagome compounds like AV_3Sb_5 [43]. In this case, electronic correlations might overtake the phononic contribution and lead to an ordered state irrespective of a subsequent phonon anomaly.

To give a first estimate on the experimental feasibility of CsCu_3Cl_5 , we perform DFT phonon calculations at the Γ -point within the harmonic approximation (cf. *Computational Methods* for further details on the calculation). The pristine configuration exhibits imaginary phonon modes, confirming the metastable state. In con-

trast, the twisted configuration yields 24 stable optical phonons modes with frequencies ranging from 0.68 to 7.14 THz. Although restricted only to $q = \Gamma$, this phonon analysis provides a first indication of a possible stability of the twisted configuration.

Wannier Model of twisted CsCu_3Cl_5

Since the twisted configuration is energetically favorable, we additionally derive the Wannier model for this structure. The band structure of the twisted kagome compound closely resembles that of the pristine case, allowing for the construction of a qualitatively equivalent Wannier model using the same orbitals and local axis orientation (see *Local frame of reference* above). In the twisted structure, however, Cu and Cl atoms no longer lie in the same plane. As a result, the Wannier orbital lobes are also displaced from the plane and exhibit a slight tilt of approximately 12° . Despite this geometric distortion, the orbital remains centered on the Cu site and retains a similar shape, originating from a linear combination of the Cu $d_{x^2-y^2}$ orbital, the neighboring Cl p orbitals, and a small contribution from the nearest-neighbor Cu $d_{x^2-y^2}$ orbitals. Rotational symmetry is now limited to 120° rotations implying the reduced $P\bar{6}2m$ space group, while retaining the same unit cell, with fractional atomic coordinates listed in Tab. SII. The band structure obtained from this three-orbital tight-binding model shows excellent agreement with the DFT results, as illustrated in Fig. S5(c), with minimal spread in the Wannier functions. This validates the use of MLWFs and confirms that the three-orbital model offers a compact and reliable basis for many-body calculations, even in the twisted configuration. Using these MLWFs as the target subspace for cRPA calculations yields a screened on-site Coulomb interaction of $U_{eff} = 3.3$ eV. This slightly reduced value compared to the pristine case is consistent with the band structure, where two bands located below the kagome manifold lie closer in energy and contribute additional screening. Combined with a narrower bandwidth, this leads to a ratio $U/t \approx 5.3$, indicating a modest increase in electronic correlations.

Atom	a	b	c
Cs1	0.000	0.000	0.000
Cu1	0.418	0.418	0.500
Cu2	0.582	0.000	0.500
Cu3	0.000	0.582	0.500
Cl1	0.000	0.000	0.500
Cl2	0.667	0.333	0.732
Cl3	0.333	0.667	0.268
Cl4	0.333	0.667	0.732
Cl5	0.667	0.333	0.268

TABLE SII. Atomic positions of twisted CsCu_3Cl_5 in direct coordinates.

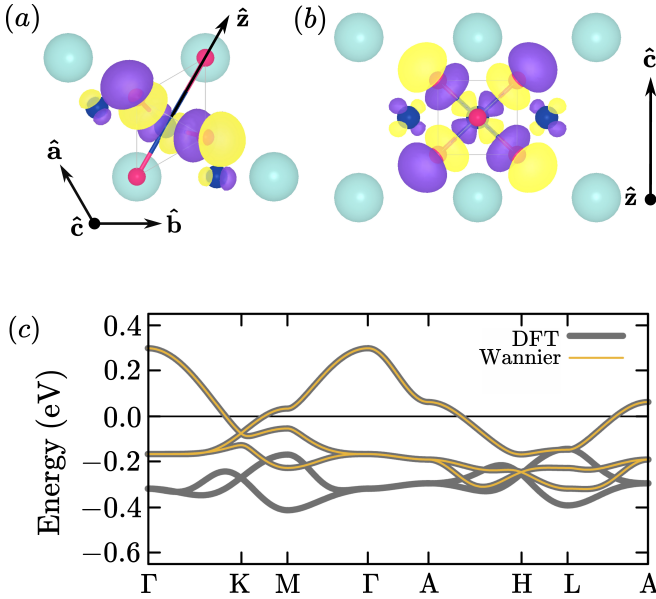


FIG. S5. (a) Top and (b) side views of the Wannier orbital centered on the Cu site in the twisted structure. The site-local reference axis \hat{z} points toward the center of the hexagonal plaquettes. The purple and yellow lobes indicate the phase of the MLWF. (c) Band structure comparison between DFT (gray) and the three-orbital Wannier tight-binding model (yellow).

COMPUTATIONAL METHODS

Density Functional Theory

Electronic structure calculations were performed with the Vienna Ab Initio Simulation Package (VASP) [69, 70], using the projector augmented wave (PAW) method. Generalized Gradient Approximation (GGA), within the Perdew-Burke-Ernzerhof (PBE) method, has been used to handle exchange and correlation effects [71]. Volume and structural relaxations have been computed with a plane-wave cutoff of 500 eV. The relaxation of the electronic degrees of freedom was considered converged when the energy difference between two steps was equal or smaller than $1.0e^{-8}$ eV. The ionic relaxation loop was considered converged when the norms of the forces acting on all atoms were equal or smaller than $1.0e^{-6}$ eV/Å. The number of k -points was set to $18 \times 18 \times 12$, both for relaxation and self-consistent loop. Partial occupancies have been determined according to a Gaussian smearing, with a width of 0.05 eV. Band structures results have been visualized using the VASPKIT postprocessing tool [72], while VESTA [73] has been used to visualize crystal structures and charge density isosurfaces. Wannier models have been constructed by using the WANNIER90 package [74]. The data of all calculations can be accessed on the Zenodo platform [75].

Constrained Random Phase Approximation

We obtained interaction parameters from first-principles electronic structure calculations, employing the constrained random phase approximation (cRPA) as implemented in VASP [70, 76], based on WANNIER90 [74] and the VASP2WANNIER90 interface. The calculations were performed using a $9 \times 9 \times 6$ k -point mesh, a plane-wave energy cutoff of 600 eV, a 400 eV cutoff for the response functions and approximately 200 unoccupied bands. Consistent with the underlying DFT calculations, the PBE exchange-correlation functional was used throughout, a Gaussian smearing of 0.05 eV was applied, and total energies were converged to within 10^{-8} eV.

In cRPA, the interaction tensor inside the correlated manifold is obtained by considering the screening effect of all other bands on the Coulomb repulsion: These rest bands provide a background whose polarizability is evaluated by calculating the bare particle-hole susceptibility within linear response theory. This polarization bubble is then inserted in a Dyson equation for the dielectric screening of the Coulomb repulsion leading to renormalized interaction parameter in the target space.

In addition to the missing contribution from diagrammatic screening processes outside the RPA ladder series, the incomplete disentanglement between the low-energy subspace (target space) and the higher-energy bands poses additional difficulties for reliable cRPA calculations: The bands generated from the MLWFs, which are used to define the target space, overlap with other lower-lying bands, thereby undermining the assumption that high-energy states can be cleanly integrated out. This leads in particular to a high sensitivity to the calculation parameters impeding quantitative estimates of the interaction strength. For a detailed discussion of the drawbacks of the cRPA approximation we refer to Ref. [77–79]. Hence, we employ the obtained cRPA parameter as a qualitative estimate for the degree of correlations in CsCu_3Cl_5 compared to other kagome compounds as discussed in the main paper. Remarkably, this classification is consistent with the intuitive bond length analysis presented above reassuring the initial assessment of CsCu_3Cl_5 as an intermediately correlated kagome material. Notably, the obtained U/V ratio is consistent with the universal scaling behavior of long-range screened Coulomb interaction obtained in independent cRPA studies on V-based kagome compounds [30].

Functional Renormalization Group

Kagome materials exhibit a variety of competing electronic instabilities, which can intertwine in complex ways. To identify possible ordering tendencies without bias, a method capable of capturing all channels on equal footing is required. For this purpose, we employ the func-

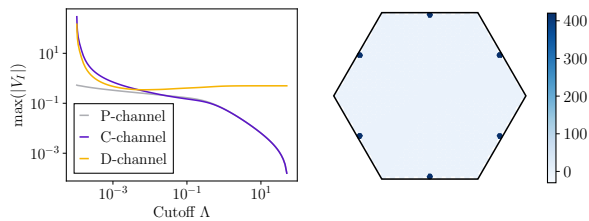


FIG. S6. Representative FRG analysis for the pristine model with bare interaction vertex defined in Eq. (1) of the main paper with $U = 0.5$ eV and $V = 0.25$ eV. (left) Flow of the maximal vertex element in the three channels. The divergent C channel indicates a magnetic instability. (right) Eigenvalue spectrum of the C channel vertex at the end of the flow. The system exhibits degenerate instabilities at each of the three M points, that are symmetry related by a C_3 rotation. The three corresponding eigenvectors are depicted in Fig. S8.

tional renormalization group (FRG) [47, 48].

The FRG solves the many electron problem by parametrizing the flow of the effective action by an artificial cutoff Λ from a solvable bare theory ($\Lambda \rightarrow \infty$) to the full interacting system ($\Lambda = 0$). This is achieved by dressing the bare propagators with a Λ dependent regulator, that selectively suppresses electronic modes in the partition sum. In general, this flow is described by an infinite set of integro-differential equations containing all kinds of higher order screening processes. To arrive at a computationally feasible problem, the hierarchy of diagrams is truncated at the one loop level, *i.e.* only screening processes involving the effective two particle interaction are kept in the equations. While this restricts the FRG to the weak to intermediate coupling regime, where the 1-loop approximation is valid, it allows to write the FRG flow equations in a closed form and numerically solve them. In order to do so, we use the truncated unity (TU) parametrization of FRG to separate the flow of the full vertex \mathcal{V} into the three diagrammatic channels according to the momentum transfer \mathbf{q} of the fermionic loop integrals: the particle-particle (P), direct particle-hole (D) and crossed particle-hole (C) channel [80–82]. The flow is stopped upon encountering a divergence in one of the channels, that indicates a superconducting (P), charge (D) or magnetic (C) instability. The predicted phase transition is determined by solving the linearised gap equation in the divergent channel, that amounts to an eigenvalue equation: The eigenvector corresponding to the leading eigenvalue gives the order parameter in the symmetry broken phase.

$$\lambda(\mathbf{q})\Delta_f(\mathbf{q}) = \sum_{f'} \mathcal{V}_{ff'}^{\text{P/C/D}}(\mathbf{q}) \Delta_{f'}(\mathbf{q}). \quad (\text{S1})$$

Here, we suppressed all other potential indices. In TUFGR, this eigenvector is given in terms of the ordering vector \mathbf{q} equal to the center of mass momentum of the fermionic bilinear and the real space relative coordinate

on the crystal lattice f . An archetypical flow and the resulting eigenvalue spectrum $\lambda(\mathbf{q})$ in the BZ is depicted in Fig. S6.

The FRG calculations were performed with the TUFGR backend of the divERGE library [46]. We employed a 30×30 mesh for the bosonic momenta of the vertices, with an additional refinement of 61×61 for the integration of the loop. The form-factor cutoff distance is chosen as 1.99 in units of the lattice vectors. We check for convergence by calculating selected points in parameter space with increased number of momentum points and form-factor cutoff (42×42 , refinement: 81×81 , formfactor cutoff: 3.32). We utilized the Euler 34 integrator of the divERGE library.

Taking into account the importance of long-range interactions on the kagome, we employ on-site and nearest neighbour density-density interactions via the interaction Hamiltonian Eq.(3) in the main text. As discussed above, the absolute interaction values of the cRPA are not trustworthy. Consequently, we perform a phase scan in U and V to determine the system's symmetry breaking propensities for a wide range of interaction scenarios presented in Fig. S7. For the pristine case, the abundant order in the reasonable interaction regime $U > V$ is given the spin bond order discussed in the main text. In the FRG, this surfaces as divergent vertex at $\mathbf{q} = M_i \forall i = 1, 2, 3$ (compare Fig. S6).

For the twisted configuration, the broken C_6 symmetry significantly reduces the Fermi surface nesting away from the vHs points. This leads to a suppression of emergent orders in the $U < V$ regime and favor weak coupling superconductivity at sufficiently strong U . However, still the SBO phase persists in the stronger correlated part of the phase diagram around the U/V ratio predicted by cRPA. Hence, we conclude that critical fluctuations in CsCu_3Cl_5 are still of SBO type and the lattice distortion only marginally effects the material's symmetry breaking behavior.

The results shown in the main part of this work were obtained with representative interaction values $U = 0.5$ eV and $V = 0.25$ eV close to the U/V ratio from cRPA.

Ginzburg-Landau Analysis of the 3Q Order

The FRG calculations exhibit a divergent susceptibility simultaneously at the three inequivalent M - points in the hexagonal Brillouin zone indicating a phase transition with the given wave vector (cf. Fig. S6). Solving the linearised gap equation at the phase transition for the three different ordering vectors gives the pattern displayed in Fig. S8, where we only depict the most dominant nearest neighbor bond magnetisation and neglect longer range bonds for clarity. To determine the relative strength of the degenerate ordering vectors, we consider coupling between the different ordering vectors by means

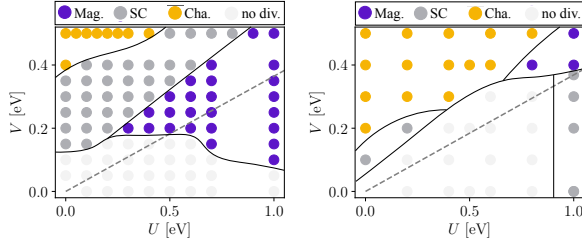


FIG. S7. FRG phase diagram for CsCu₃Cl₅ in the pristine (left) and twisted (right) configuration as a function of interaction values U and V defined in Eq. (1) in the main paper. Different colors indicate magnetic (mag.), charge (Cha.) and superconducting (SC) instabilities. Light grey marks points without a divergent susceptibility, *i.e.* no symmetry breaking within the resolution of the calculation. Solid black lines denote the approximate phase boundaries, while dashed black lines indicate the U/V ratio obtained from cRPA.

of Ginzburg-Landau (GL) theory at the Fermi level. In contrast to the previously studied $3Q$ charge orders on the kagome lattice (see *e.g.* Ref. [40]), the relative orientation of the magnetic ordering vector per Q adds three continuous degrees of freedom to the relative strength and sign of the three independent order parameters subject to the GL analysis. To obtain the free energy functional after the FRG flow and avoid double counting, we project the interacting theory at the FRG cutoff scale onto the three van Hove momenta, which carry the dominant spectral weight on the Fermi surface [59, 83]. The prevalent contribution to this Hamiltonian is given by the most divergent part of the FRG vertex, that we expand up to second order in the fluctuations around the static order parameter using a Hubbard-Stratonovich transformation. The resulting action for the low energy effective theory on the Fermi level reads

$$S = -T \sum_{\omega_n} \sum_{\alpha s} c_{\alpha s}^\dagger(\omega_n) G_\alpha(\omega_n) c_{\alpha s}(\omega_n) + \sum_{\alpha\beta\gamma} \epsilon_{\alpha\beta\gamma} \vec{\Delta}_\gamma \vec{S}_{\alpha\beta}(\omega_n) + g^{-1} \sum_{\gamma} \vec{\Delta}_\gamma^2, \quad (\text{S2})$$

with the non-interacting Green's function $G_\alpha(\omega_n) = 1/(i\omega_n - \varepsilon_\alpha)$ and the spin operator $\vec{S}_{\alpha\beta}(\omega_n) = \sum_{ss'} c_{\alpha s}^\dagger(\omega_n) \vec{\sigma}^{ss'} c_{\beta s}(\omega_n)$, where $\vec{\sigma}$ are Pauli matrices acting on spin space, and the sum runs over all fermionic Matsubara frequencies ω_n . Due to the mixed orbital content of the vHS, there is no one-to-one correspondence between the vH index α and the sublattice degree of the original TB model opposed to the p -type scenario [83]. However, the scattering in the magnetic channel is purely off-diagonal in this new basis analogous to the p -type scenario, since the different instabilities $\vec{\Delta}_\gamma = \Delta(M_\gamma)$ for $\gamma \in \{1, 2, 3\}$ involve a momentum transfer between the different vHS points at M_α, M_β with $\alpha \neq \beta \neq \gamma$. By carrying out the Gaussian integrals in the remaining

Grassman fields, one obtains the free energy

$$F = g^{-1} \sum_{\gamma} \vec{\Delta}_\gamma^2 - \text{Tr} \ln(-\mathcal{G}^{-1}) \quad (\text{S3})$$

where we define the fully interacting Green's function $\mathcal{G}^{-1} = G^{-1} + \Sigma^{-1}$ in the tensor product Hilbert space of spin and patch degrees of freedom, *i.e.* $G = 1_{2 \times 2} \otimes \text{diag}(G_1, G_2, G_3)$ and

$$\Sigma = \begin{pmatrix} 0 & \vec{\Delta}_3 & -\vec{\Delta}_2 \\ -\vec{\Delta}_3 & 0 & \vec{\Delta}_1 \\ \vec{\Delta}_2 & -\vec{\Delta}_1 & 0 \end{pmatrix}. \quad (\text{S4})$$

Each $\vec{\Delta}_\gamma$ is hence a 2×2 matrix in spin space, whose Pauli vector is kept as tuning parameter. Expanding the free energy in terms of the order parameter fields up to fourth order we obtain the GL functional

$$F = g^{-1} \sum_{\gamma} \vec{\Delta}_\gamma^2 + \frac{1}{2} \text{Tr}(G\Sigma)^2 + \frac{1}{4} \text{Tr}(G\Sigma)^4 + \mathcal{O}(\Sigma^6), \quad (\text{S5})$$

that is valid in vicinity of the phase transition. The quadratic order

$$F^{(2)} = \sum_{\gamma} \left(\frac{1}{g} - \chi^{ph}(T) \right) \vec{\Delta}_\gamma^2 \propto T - T_c, \quad (\text{S6})$$

is given by the non-interacting particle-hole susceptibility $\chi^{ph}(T) = \text{Tr}(G_1 G_2)$ and scales linear around the transition temperature T_c . Since the free energy inherits time-reversal and global SO(3) symmetry of the spin quantisation axis from the kinetic Hamiltonian Eq. (1) in the main text, the cubic term is absent and a coupling of the different order parameter $\vec{\Delta}_\gamma$ first appears at quartic order

$$F^{(4)} = Z_1 \left(\sum_{\gamma} \vec{\Delta}_\gamma^2 \right)^2 + 2(Z_2 - Z_1 - Z_3) \left(\vec{\Delta}_1^2 \vec{\Delta}_2^2 + \vec{\Delta}_2^2 \vec{\Delta}_3^2 + \vec{\Delta}_3^2 \vec{\Delta}_1^2 \right) + 4Z_3 \left((\vec{\Delta}_1 \cdot \vec{\Delta}_2)^2 + (\vec{\Delta}_2 \cdot \vec{\Delta}_3)^2 + (\vec{\Delta}_3 \cdot \vec{\Delta}_1)^2 \right). \quad (\text{S7})$$

The expansion coefficients can be calculated from the kinetic theory on the Fermi level and are given by

$$\begin{aligned} Z_1 &= \text{Tr}(G_1^2 G_2^2), \\ Z_2 &= \text{Tr}(G_1^2 G_2 G_3), \\ Z_3 &= \text{Tr}(G_1 G_2 G_3 G_0). \end{aligned} \quad (\text{S8})$$

These prefactors can be calculated analytically by expanding the TB bandstructure around the saddle-points; the resulting action is identical to that of Ref. [84]. While $Z_2 - Z_1 - Z_3 < 0$ results in an equal strength of the three magnetic ordering vectors, $Z_3 < 0$ aligns the magnetisation vectors of the different $\vec{\Delta}_\gamma$. This uniaxial spin

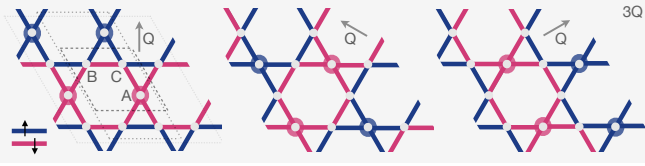


FIG. S8. Three symmetry equivalent magnetic orders with largest susceptibility in the FRG flow given by the eigenvectors corresponding to the leading eigenvalues of Fig. S6. Colored sites (bonds) indicate a finite local magnetisation on the associated site (bond). Dotted (dashed) polygons indicate the extended (original) unit cell corresponding to the translation symmetry breaking indicated by Q . All NN bonds share the same absolute value of the magnetization with sign structure indicated by different colors. More distant bonds likewise display a finite magnetization but with absolute values of 2 orders of magnitude smaller in size and are hence not shown. The relative strength of on-site and bond magnetization is highly dependent on the phase space point in Fig. S7 and hence only schematically drawn here.

arrangement of the $3Q$ state persists within the symmetry broken phase as evidenced by the sixth order term $F^{(6)} = -4Z_4(\vec{\Delta}_1 \cdot \vec{\Delta}_2 \times \vec{\Delta}_3)^2$ with $Z_4 < 0$ [84]. The final result of the combined FRG and GL analysis is presented in Fig. 3 in the main text and resembles other itinerant SDW patterns on the kagome lattice Hubbard model discussed in the literature [12, 13, 46, 83, 85].

The real space order parameter of the parent spin bond order phase determined by our FRG analysis breaks Z_4 translation symmetry and time reversal symmetry \mathcal{T} . Since the global spin quantisation axis remains undefined, the magnetic states can be classified by the irreducible representations (irreps) of the magnetic space group $\mathcal{M} = C_{6v}''' \otimes \mathcal{T}$, that is a direct product of enlarge space group in the 2×2 unit cell and TRS symmetry. The $\vec{\Delta}_\gamma^{SDW/SBO}$ obtained by the presented GL analysis transforms within the F_2' irrep, where the prime indicates an odd transformation behaviour under the TRS \mathcal{T} . This results from an F_1 structure for the spatial part of the order parameter combined with an odd transformation behaviour of the spin degree of freedom under all mirror operations (corresponding to an A_2 irrep for the spin part). Despite Eq. (S7) does not determine the spin polarisation value along the unidirectional quantisation axis, all possible parallel and antiparallel magnetic arrangements of the different $\vec{\Delta}_\gamma$ result in the same physical state, potentially translated by one original kagome lattice vector, that constitute the three basis states of the F_2' irrep.

As a direct consequence, the uniaxial spin alignment of the obtained $3Q$ order differs drastically from studies of the kagome Heisenberg model, that suggests an octahedral order as preferred superposition of the different $\vec{\Delta}(M_\gamma)$ ordering vectors [86]. The reason for this apparent discrepancy roots in the dissimilar nature of the

coupling between the 3 ordering vectors: In the kagome Heisenberg model, the different orders interact via the bare short-range first and second nearest-neighbor spin-exchange couplings J_1 and J_2 . In the itinerant picture, however, these couplings are generated dynamically and are driven by bandstructure effects, namely the pronounced nesting of the M -point vHS.

EMERGENCE OF OCTAHEDRAL ORDER INSIDE THE COLLINEAR MAGNETIC PHASE

Within the symmetry broken phase, the spin exchange coupling is expected to become larger as the GL expansion breaks well below the Néel temperature T_N and eventually promote a perpendicular spin orientation of the different $\vec{\Delta}_\gamma$ in accordance with self-consistent mean field calculations on the honeycomb lattice [84]. This tendency can be directly inferred from the highest order GL term considered above: Exploiting the universal relation $|\vec{\Delta}_\gamma|_{T=0} \propto T_N$, we can reevaluate the prefactors Z_i of the GL functional at low temperatures in the limit $T_N \lesssim t$ with t is the kinetic energy scale of the system to obtain an intuition of the leading coupling terms between the magnetic ordering vectors. We recognize, that Z_4 changes sign already at small values of T_N , thus favoring a pairwise orthogonal orientation of the magnetic vectors $\vec{\Delta}_\alpha \perp \vec{\Delta}_\beta \perp \vec{\Delta}_\gamma \perp \vec{\Delta}_\alpha$ [84]. We thus recover the octahedral spin order deep inside the magnetic phase, that is separated from the uniaxial F_2' order by a first order transition. As discussed in the main text, the non uniaxial spin order couples linearly to spin loop current order, immediately inducing a coexisting spin current order.

Property	CsCu ₃ Cl ₅	CsCu ₃ Cl ₄ Br	CsCu ₃ Cl ₄ I
$ \hat{c} $ (Å)	7.027	7.179	7.494
$E_{\text{vHS},m}$ (eV)	0.06	0.03	-0.04
$\Delta E_{\text{vHS},m}$ (eV)	0.26	0.22	0.15

TABLE SIII. Comparison of structural and electronic properties for CsCu₃Cl₅, CsCu₃Cl₄Br, and CsCu₃Cl₄I. $|\hat{c}|$ represents the length of the unit vector perpendicular to the kagome plane, while $E_{\text{vHS},m}$ indicates the energy of the m -type vHS relative to the Fermi level. $\Delta E_{\text{vHS},m}$ denotes its shift in energy from the M -point to the L -point in k-space.

THE ROLE OF THE k_z -DISPERSION

Due to the layered structure of the compound, we have conducted FRG calculations in the $k_z = 0$ plane, thus omitting the dispersion in the third direction in accordance with other theoretical studies, *e.g.* on AV₃Sb₅ [57]. CsCu₃Cl₅ exhibits some hybridization along the k_z direction, introducing out-of-plane dispersion in the bandstructure that softens the logarithmic divergence in the

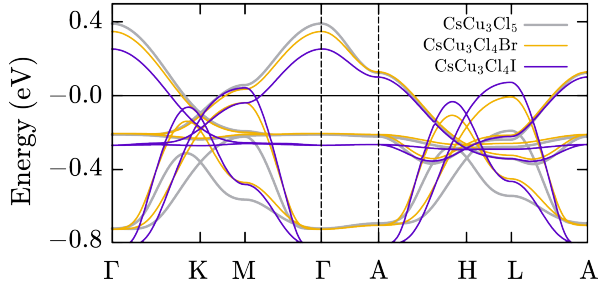


FIG. S9. Comparison of band structures of different Cu based kagome compounds illustrating the effects of increasing substituting atom size on the kagome bands. As the substituting atom size increases, the kagome bands narrow and shift downward in energy, while the other two bands broaden and shift upward.

density of states at the 2D van Hove points.

A future goal is to enhance the two-dimensional characteristics of the layered material by either effectively screening interlayer hopping or by increasing the interlayer spacing between the planes along the z -axis. The latter can be approached in two ways. First, the thickness of the triangular layer can be increased by substituting Cs with a molecule that has a +1 oxidation state, or by adding a neutral molecule to the layer. To preserve the unique kagome physics, it is essential that any added structures maintain kagome symmetry and are carefully examined to ensure that the m -type vHS remain close to the Fermi level. The second approach involves increas-

ing the spacing between the kagome Cu_3Cl layer and the chlorine layers that sandwich it. This can be achieved by substituting the Cl atom at the Wyckoff position 1b with larger elements from the same group, such as Br or I. The k_z dispersion can be measured by the change in energy of the vHS between the M -point ($k_z = 0$) and the L -point ($k_z = 1/2$).

Fig. S9 compares the band structures of CsCu_3Cl_5 , $\text{CsCu}_3\text{Cl}_4\text{Br}$, and $\text{CsCu}_3\text{Cl}_4\text{I}$. As the size of the substituting atom increases, the kagome bands narrow and shift downward in energy, while the other two bands widen and shift upward. To quantify the effects of substitution, Tab. SIII lists the length of the \hat{c} unit vector perpendicular to the plane, the position of the m -type vHS in the $k_z=0$ plane relative to the Fermi energy, and the change in energy of this vHS from $k_z=0$ to $k_z=1/2$ for the different substitutions. Comparing these values shows that as the substituting atom increases in size, the \hat{c} out-of-plane unit vector indeed grows, decreasing interlayer hopping and reducing k_z -dispersion. For example, substituting with Iod increases the unit cell size along the \hat{z} -direction from 7.027 Å to 7.494 Å and reduces the k_z dispersion of the m -type vHS from 0.26 eV to 0.15 eV. The vHS shifts from 0.06 eV above the Fermi level to 0.04 eV below it. As observed for CsCu_3Cl_5 , orbital projections show that the three characteristic kagome bands originate from Cu $d_{xz} + d_{yz} + \text{Cl } p$ orbitals. The Iod p -orbitals only contribute to the two lower bands in Fig. S9. Projections onto the single Cu atoms confirm the presence of sublattice interference.